

Dynamic modelling of passive margin salt tectonics: effects of water loading, sediment properties and sedimentation patterns

Lykke Gemmer,* Christopher Beaumont* and Steven J. Ings†

*Geodynamics Group, Department of Oceanography, Dalhousie University, Halifax, NS, Canada

†Department of Earth Sciences, Dalhousie University, Halifax, NS, Canada

ABSTRACT

We investigate the evolution of passive continental margin sedimentary basins that contain salt through two-dimensional (2D) analytical failure analysis and plane-strain finite-element modelling. We expand an earlier analytical failure analysis of a sedimentary basin/salt system at a passive continental margin to include the effects of submarine water loading and pore fluid pressure. Seaward thinning sediments above a weak salt layer produce a pressure gradient that induces Poiseuille flow in the viscous salt. We determine the circumstances under which failure at the head and toe of the frictional–plastic sediment wedge occurs, resulting in translation of the wedge, landward extension and seaward contraction, accompanied by Couette flow in the underlying salt. The effects of water: (i) increase solid and fluid pressures in the sediments; (ii) reduce the head to toe differential pressure in the salt and (iii) act as a buttress to oppose failure and translation of the sediment wedge. The magnitude of the translation velocity upon failure is reduced by the effects of water.

The subsequent deformation is investigated using a 2D finite-element model that includes the effects of the submarine setting and hydrostatic pore pressures. The model quantitatively simulates a 2D approximation of the evolution of natural sedimentary basins on continental margins that are formed above salt. Sediment progradation above a viscous salt layer results in formation of landward extensional basins and listric normal growth faults as well as seaward contraction. At a later stage, an allochthonous salt nappe overthrusts the autochthonous limit of the salt. The nature and distribution of major structures depends on the sediment properties and the sedimentation pattern. Strain weakening of sediment favours landward listric growth faults with formation of asymmetric extensional depocentres. Episodes of low sediment influx, with partial infill of depocentres, produce local pressure gradients in the salt that result in diapirism. Diapirs grow passively during sediment aggradation.

INTRODUCTION

Salt tectonics occurs in several passive continental margin sedimentary basins, for instance the US Gulf of Mexico (e.g. Worrall & Snelson, 1989; Wu *et al.*, 1990; Diegel *et al.*, 1995; Peel *et al.*, 1995; Trudgill *et al.*, 1999; Rowan *et al.*, 2000), the margin offshore Brazil (e.g. Demercian *et al.*, 1993; Cobbold *et al.*, 2001b; Modica & Brush, 2004), margins offshore west Africa (e.g. Duval *et al.*, 1992; Marton *et al.*, 2000; Tari *et al.*, 2002) and the Atlantic Canadian margin (e.g. Wade & MacLean, 1990; Yassir & Bell, 1994; Kidston *et al.*, 2002; Shimeld, 2004). These provinces are characterised by salt overlain by seaward thinning sediment layers resulting from seaward progradation of sediments from adjacent onshore regions (e.g. Fig. 1). The sediments are characterised by regions of landward exten-

sion beneath the shelf and seaward contraction (e.g. Tari *et al.*, 2002). This configuration has been attributed to differential sediment loading of a viscous salt layer, which leads to seaward flow of the salt and in many instances the overlying sediments (e.g. Worrall & Snelson, 1989). The timing of salt deposition relative to rifted margin formation, sedimentation patterns, and the effects of regional tectonic events are highly variable from province to province (e.g. Tari *et al.*, 2002). Figure 1 shows an interpreted seismic section from the Santos Basin on the margin offshore Brazil (modified after Modica & Brush, 2004) where salt tectonics has significantly affected the structural evolution. Following deposition of Aptian salt, sediment progradation lead to seaward salt evacuation, which caused the formation landward extensional faults and seaward broad salt diapirs and salt-cored folds at the toe of the slope.

Previous models have investigated the distribution of major tectonic structures in passive margin salt basins. Lehner (1977, 2000) used an analytical model to investigate systems in which the pressure gradient in the viscous salt

Correspondence, present address: Lykke Gemmer, Earth Sciences, School of Earth and Environment, University of Leeds, Leeds LS2 9JT, UK. E-mail: lykke@earth.leeds.ac.uk

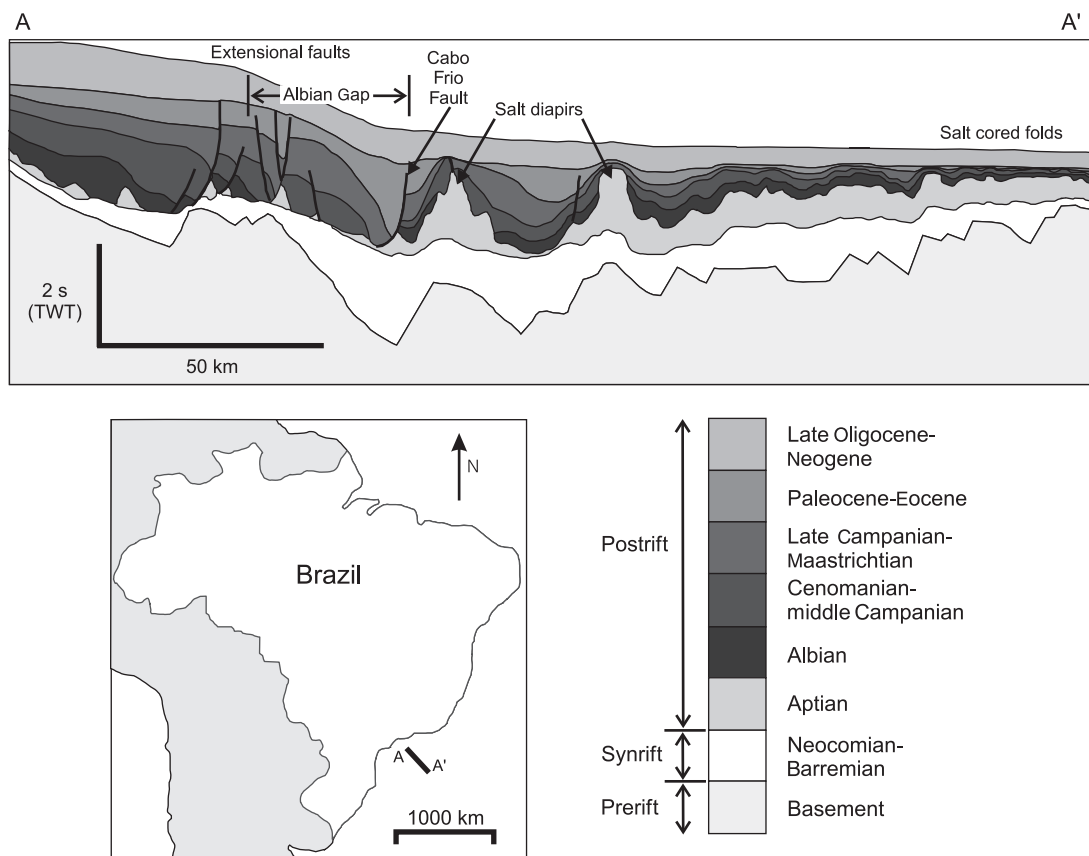


Fig. 1. Interpreted seismic section across the Central Santos Basin, offshore Brazil showing some of the typical salt tectonic structures observed on passive continental margins (after Modica & Brush, 2004). Seaward evacuation of Aptian salt has led to extensional faults in the landward region and broad salt diapirs and salt cored-folds at the toe of the slope. Extension localised on the Cabo Frio Fault resulted in a broad zone of rollover (Albian Gap).

drives deformation under a passive overburden and he subsequently considered the stability of the overburden treated as a frictional–plastic material. For given overburden and salt geometries, the overburden is just below the frictional yield limit for a certain choice of overburden strength. Any reduction of the overburden strength below this value results in overburden failure, leading to seaward flow of the overburden and regions of extension and contraction bounding the overburden slope. The deformation of the system during overburden flow has been investigated through analogue (e.g. Vendeville & Jackson, 1992; Koyi, 1996; Ge *et al.*, 1997; Cotton & Koyi, 2000) and numerical models (e.g. Last, 1988; Cohen & Hardy, 1996) of viscous material beneath a brittle overburden. These models have demonstrated the general pattern of landward extension and seaward contraction in systems that undergo sediment progradation and aggradation over a viscous salt substratum.

Although most passive margin salt basins evolve in a submarine environment, few modelling studies consider the effects of the water on the evolution of the margin systems (e.g. Fletcher *et al.*, 1995; Cobbold *et al.*, 2001a; Mourgues & Cobbold, 2003; Vendeville & Gaullier, 2003). Cobbold *et al.* (2001a), Mourgues & Cobbold (2003) and Vendeville & Gaullier (2003) used analogue models to in-

vestigate the effects of pore fluid pressures in the sediments and showed that pore overpressures may have significant effects on slope stability and hence on the dynamics of continental margin sedimentary basins.

Gemmer *et al.* (2004) used an analytical model and two-dimensional (2D) plane-strain finite-element experiments to study a uniform thickness linear-viscous layer overlain by a frictional–plastic sedimentary overburden that decreases in thickness from the proximal to distal limits of the salt (i.e. a progradational wedge configuration). They used thin-sheet horizontal force balance analysis to predict the circumstances under which the sedimentary overburden would fail and estimated the initial velocities of the failing overburden. In this paper, we expand the analysis to include the effects of water load and sediment pore fluid pressures. In addition, we use finite-element experiments that include water loading and hydrostatic pore fluid pressures in the sediments to investigate the finite deformation of the system.

Gemmer *et al.* (2004) investigated the sensitivity of the systems to the width of the salt layer and the role of sedimentation and sediment progradation rate. Ings *et al.* (2004) expanded on this work and investigated the roles of a regional seaward tilt of the salt layer, isostatic adjustment under the prograding sediment load and the effects

of salt buoyancy. Here we analyse the effects of sediment properties and show how strain-dependent weakening of the sediments affects the system. In addition we investigate the effects of more complicated sedimentation patterns, such as periods of low sediment influx, sediment aggradation and sediment bypass of depocentres. All models considered in this study are 2D plane-strain models and it should be emphasised that this limits us to investigate systems where no out-of-plane deformation occurs.

FAILURE ANALYSIS

When a viscous substrate is overlain by a frictional–plastic overburden of laterally varying thickness the differential load of the overburden causes a pressure gradient and Poiseuille flow in the viscous material (Fig. 2a). Under some circumstances the overburden reaches its yield limit and fails by landward extension and seaward contraction and the overburden translates in the seaward direction (Fig. 2b). In this case, both Poiseuille and Couette flow occur in the viscous channel and the relative amplitudes of the two flow types determine the dominant style of viscous flow. For cases with very unstable overburden, Couette flow will dominate in the viscous channel (Fig. 2b). For mildly unstable systems the Couette velocity may be smaller than or of the same order of magnitude as the Poiseuille velocity and a combination of the two flow types will characterise the deformation.

Lehner (2000) and Gemmer *et al.* (2004) investigated the circumstances under which the overburden will fail and the initial velocities of the failing overburden for plane-strain systems. Here we summarise these derivations and then show how they can be expanded to take into account the effects of water loading and pore fluid pressures. To represent a simple passive continental margin sedimentary basin with a salt layer overlain by a seaward thinning sediment wedge, we consider 2D vertical plane-strain initial configurations, like those of Fig. 2. The base is horizontal and a linear viscous layer has a uniform thickness beneath

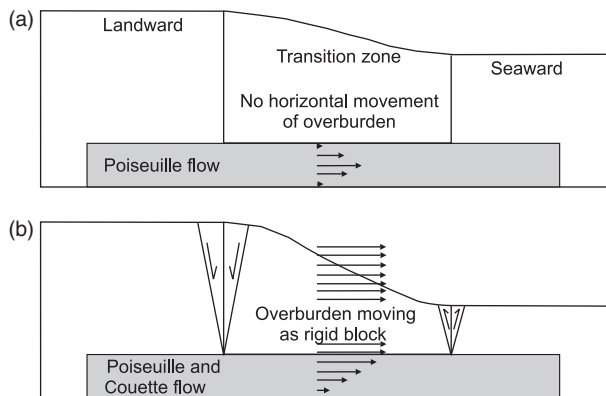


Fig. 2. Deformation styles. (a) Overburden below yield. Poiseuille flow in viscous channel. (b) Overburden at yield. Couette flow and Poiseuille flow in viscous channel.

a variable thickness frictional–plastic overburden. For this simple system, no consideration is given to the way in which the geometry was created.

Case 1. No water loading

In this section we consider the case where no water loading or pore fluid pressure effects are taken into account (Lehner, 2000; Gemmer *et al.*, 2004). Consider the horizontal forces that act on the overburden transition zone outlined by the thick line (Fig. 3a). The upper surface is stress free and the forces F_1 and F_2 result from the vertically integrated horizontal stresses in the frictional overburden. The pressure-driven Poiseuille flow in the viscous layer produces shear traction on the base of the overburden resulting in the horizontal force F_p . In addition, the Couette flow causes a basal traction force, F_c , when the overburden fails and moves horizontally. When the overburden is at yield, these horizontal forces must balance

$$F_1 + F_2 + F_p + F_c = 0. \quad (1)$$

F_1 and F_2 are the forces that result from the landward tensional and seaward compressional horizontal stresses in the yielding plastic overburden, above locations x_1 and x_2 . The Mohr–Coulomb criterion is used to represent the noncohesive frictional–plastic behaviour of the overburden

$$\sigma_{zz} - \sigma_{xx} = (\sigma_{xx} + \sigma_{zz}) \sin \phi \quad (\text{extension}) \quad (2a)$$

$$\sigma_{zz} - \sigma_{xx} = -(\sigma_{xx} + \sigma_{zz}) \sin \phi \quad (\text{contraction}) \quad (2b)$$

where σ is stress and ϕ is the internal angle of friction. We assume that the principal stresses in the overburden are horizontal (σ_{xx}) and vertical (σ_{zz}) and that σ_{zz} is the weight σ_z of the overburden (Dahlen, 1990), which gives

$$\sigma_{xx, \text{extension}} = -\rho g d \frac{(1 - \sin \phi)}{(1 + \sin \phi)} \quad (3a)$$

$$\sigma_{xx, \text{contraction}} = -\rho g d \frac{(1 + \sin \phi)}{(1 - \sin \phi)} \quad (3b)$$

where ρ is density, g is gravitational acceleration and $d = (h_c + h(x) - z)$ is depth below the surface. The resulting forces in the yielding overburden are

$$F_1 = - \int_{h_c}^{h_c+h_1} \sigma_{xx, \text{extension}} dz = \frac{1}{2} \rho g h_1^2 k \quad (4)$$

$$F_2 = \int_{h_c}^{h_c+h_2} \sigma_{xx, \text{contraction}} dz = -\frac{1}{2} \rho g h_2^2 k^{-1} \quad (5)$$

where $k = (1 - \sin \phi)/(1 + \sin \phi)$. By assuming that the topography changes slowly with position, the thin sheet approximation (Lobkovsky & Kerchman, 1991) gives the

velocity distribution in the viscous substratum subject to variations of pressure as

$$v_p = -\frac{\rho g}{2\eta} \frac{\partial h(x)}{\partial x} z(h_c - z) \quad (6)$$

where η is the viscosity. Integration over the width of the sediment wedge gives

$$\begin{aligned} F_p &= -\int_{x_1}^{x_2} \tau_p dx \\ &= -\int_{x_1}^{x_2} \eta \frac{\partial v_p}{\partial z} \Big|_{z=h_c} dx = \frac{h_c}{2} \rho g (h_1 - h_2) \end{aligned} \quad (7)$$

which is independent of the viscosity. The velocity field in the substratum, v_c , caused by horizontal motion of the upper boundary of the viscous substratum increases linearly with distance from the viscous channel base, z

$$v_c = \frac{z}{h_c} V_c \quad (8)$$

where V_c is the uniform rate of translational motion of the unstable overburden. The basal traction associated with Couette flow can be estimated as

$$\begin{aligned} F_c &= -\int_{x_1}^{x_2} \tau_c dx \\ &= -\int_{x_1}^{x_2} \eta \frac{\partial v_c}{\partial z} \Big|_{z=h_c} dx = -\eta \frac{V_c}{h_c} (x_2 - x_1). \end{aligned} \quad (9)$$

Substitution of Eqns (4), (5), (7) and (9) into Eqn. (1) gives

$$\begin{aligned} \rho g h_1^2 k - \rho g h_2^2 k^{-1} + h_c \rho g (h_1 - h_2) \\ - 2\eta \frac{V_c}{h_c} (x_2 - x_1) = 0. \end{aligned} \quad (10)$$

Dividing this relation by a reference force, $F_s = \rho g h_c^2$, results in the nondimensional equation

$$(h_1^*)^2 k - (h_2^*)^2 k^{-1} + h_1^* - h_2^* - 2V_c^* l^* = 0 \quad (11)$$

in which h_1^* , h_2^* and l^* are the nondimensional length scales $h_1^* = h_1/h_c$, $h_2^* = h_2/h_c$, $l^* = (x_2 - x_1)/h_c$, and $V_c^* = V_c/V_s$ where V_s is the scaling velocity, $V_s = \rho g h_c^2/\eta$. Eqn. (11) relates the relative overburden thicknesses, h_1^* and h_2^* , the overburden strength, expressed by k , the transition zone width, l^* , and the overburden velocity, V_c^* , for a system where the overburden is on yield. Below yield the force balance is given by Eqn. (11) or equivalently Eqn. (1) in which $V_c^* = 0$ ($F_c = 0$) and F_1 and F_2 are the below-yield values of these forces.

In the force estimations presented above, no consideration is given to the effects of pore fluid pressure on the overburden strength. A frequently used approach in modelling of sedimentary systems (e.g. Gemmer *et al.*, 2004;

Ings *et al.*, 2004) is to take into account the reduction in the effective pressure from p to $p - p_f$, where p_f is the pore fluid pressure, by defining an effective internal angle of friction, ϕ_{eff} , that is lower than the angle of friction for the dry sediment material, ϕ above. ϕ_{eff} is defined by

$$p \sin \phi_{\text{eff}} = (p - p_f) \sin \phi = p(1 - \lambda) \sin \phi \quad (12)$$

where the pore pressure ratio, $\lambda = p_f/p$, is the ratio between the fluid pressure and the solid pressure (mean stress), p . Note that the internal angle of friction of the sediment is not reduced to ϕ_{eff} ; it is just that sediment with pore pressure $p_f = \lambda \times p$, acts as though it has a yield strength that is the same as the dry system with $\phi = \phi_{\text{eff}}$. This approach is correct for systems where the pore fluid pressures are proportional to the solid pressure. Although similar, as we will show in the next sections, this approach differs from the definition of the Hubbert–Rubey pore pressure ratio in which $p = \sigma_z$ is the weight of the overburden. In regions that are under deviatoric tension or compression the true solid pressure deviates from the weight of the overburden.

Case 1 with water loading, but no pore fluid pressure effects

The effects of submarine water loading may be added to the Case 1 system described above by assuming that the water load affects the solid pressure in the sediments, but the sediment is dry and unaffected by the pore fluid pressures within the sediments. This corresponds to a system where an impermeable barrier exists between water and the underlying sediment. For simplicity, we assume that the water level is the same as the level of the surface of the landward overburden (Fig. 3b), but similar calculations could be made for the case where the water level is arbitrary.

The water, density ρ_w , acts as a load that increases the pressure and therefore the strength of the seaward overburden, which modifies the force F_2 to F_2'

$$F_2' = -\left[\frac{1}{2}\rho g h_2^2 + \rho_w g (h_1 - h_2) h_2\right] k^{-1}. \quad (13)$$

In addition, the vertical component of the water load counteracts the sediment-induced differential pressure in the viscous layer and the basal traction force caused by the Poiseuille flow, F_p , is reduced to

$$F_p' = \frac{h_c}{2} (\rho - \rho_w) g (h_1 - h_2). \quad (14)$$

Finally, because the water acts as a pressure that is normal to the surface, the horizontal component creates a buttress force that acts horizontally on the sloping overburden (Fig. 3b)

$$F_w = -\int_{h_2}^{h_1} \rho_w g z dz = -\frac{1}{2} \rho_w g (h_1 - h_2)^2. \quad (15)$$

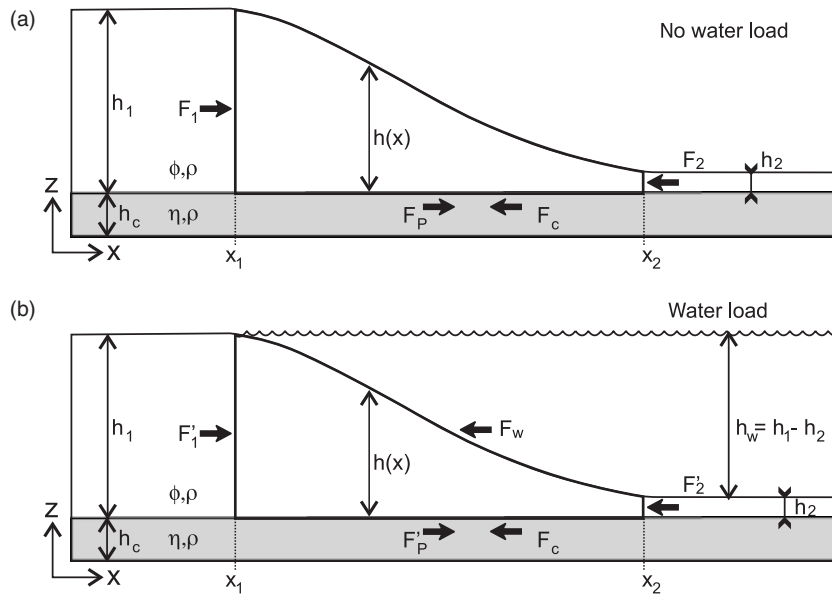


Fig. 3. Horizontal forces acting on the overburden transition zone. (a) No water loading. (b) Water loading. Overburden is white and underlying salt is grey.

The horizontal force balance equation is thus

$$F_1 + F'_2 + F'_p + F_w + F_c = 0 \quad (16)$$

which after inserting Eqns (4), (13), (14), (15) and (9) gives

$$\begin{aligned} \rho g h_1^2 k - [\rho g h_2^2 + 2\rho_w g (h_1 - h_2) h_2] t k^{-1} \\ + h_c (\rho - \rho_w) g (h_1 - h_2) - \rho_w g (h_1 - h_2)^2 \\ - 2\eta \frac{V_c}{h_c} (x_2 - x_1) = 0. \end{aligned} \quad (17)$$

Using the scaling force, $F_s = \rho g h_c^2$ to nondimensionalise this equation gives

$$\begin{aligned} (h_1^*)^2 k - [(h_2^*)^2 + 2\rho_w^* (h_1^* - h_2^*) h_2^*] k^{-1} \\ + (1 - \rho_w^*) (h_1^* - h_2^*) - \rho_w^* (h_1^* - h_2^*)^2 \\ - 2V_c^* l^* = 0 \end{aligned} \quad (18)$$

where the nondimensional parameters are $h_1^* = h_1/h_c$, $h_2^* = h_2/h_c$, $\rho_w^* = \rho_w/\rho$, $l^* = (x_2 - x_1)/h_c$, and $V_c^* = V_c/V_s$ where V_s is the scaling velocity, $V_s = \rho g h_c^2/\eta$ and $k = (1 - \sin \phi)/(1 + \sin \phi)$.

Case 2, water loading and pore fluid pressure effects

In Case 1, the effects of sediment pore fluid pressures were ignored. However, in most cases, particularly submarine passive margins, sediments contain pore fluids. The water above the sediments is connected to these pore fluids in the sediments and the pore fluid pressure is sensitive to the overlying water depth, which varies significantly across most continental margins. There is therefore a corresponding variation in effective sediment strength in

response to the spatial change in pore fluid pressure. In this section we expand the theory from Case 1 to incorporate the effects of the water load on the fluid pressures within the sediments on the assumption that pore fluid pressures are static and directly related to the weight of the overburden.

A first approximation to the pore fluid pressure may be calculated by using the Hubbert–Rubey pore pressure ratio, λ_{HR} (Hubbert & Rubey, 1959)

$$\lambda_{HR} = \frac{p_f}{\sigma_z} \quad (19)$$

where p_f is the pore fluid pressure and σ_z is the weight of the overburden. The failure analysis and velocity derivation parallels Case 1. The fluid pressures reduce the effective stress in the sediments (von Terzaghi, 1923; Mourgue & Cobbold, 2003). By taking into account the fluid pressure in the sediment but not including the weight of the water column above the sedimentary overburden, the frictional–plastic yield criterion (Eqn. (2)) therefore becomes

$$\begin{aligned} \sigma_{zz} - \sigma_{xx} = \pm (\sigma_{xx} + \sigma_{zz}) \\ \left(1 - \frac{2\lambda_{HR}\sigma_z}{\sigma_{xx} + \sigma_{zz}} \right) \sin \phi. \end{aligned} \quad (20)$$

In this case, Eqn. (3) is modified such that σ_{xx} under extensional yield is

$$\sigma_{xx} = -\rho g d \left(\frac{1 - (1 - 2\lambda_{HR}) \sin \phi}{1 + \sin \phi} \right) \quad (21a)$$

and under contraction, the yield value of σ_{xx} is

$$\sigma_{xx} = -\rho g d \left(\frac{1 + (1 - 2\lambda_{HR}) \sin \phi}{1 - \sin \phi} \right) \quad (21b)$$

where $d = (h_c + h(x) - z)$ is depth below the sediment surface and modified k 's can be defined as

$$k_w = \frac{1 - (1 - 2\lambda_{HR}) \sin \phi}{1 + \sin \phi} \quad \text{and} \quad k'_w = \frac{1 + (1 - 2\lambda_{HR}) \sin \phi}{1 - \sin \phi}. \quad (22)$$

In the case where the sediments are submerged under water, the weight of the water column modifies the yield criterion to

$$\sigma_{zz} - \sigma_{xx} = (\sigma_{xx} + \sigma_{zz}) \left(1 - \frac{2\lambda_{HR}\sigma_z}{\sigma_{xx} + \sigma_{zz}} - \frac{2\rho_w g h_w}{\sigma_{xx} + \sigma_{zz}} \right) \sin \phi \quad (\text{extension}) \quad (23a)$$

$$\sigma_{zz} - \sigma_{xx} = -(\sigma_{xx} + \sigma_{zz}) \left(1 - \frac{2\lambda_{HR}\sigma_z}{\sigma_{xx} + \sigma_{zz}} - \frac{2\rho_w g h_w}{\sigma_{xx} + \sigma_{zz}} \right) \sin \phi \quad (\text{contraction}) \quad (23b)$$

where h_w is the water depth. The seaward section in our system is submerged under water and the horizontal contractional yield stress, σ_{xx} , must therefore be estimated from Eqn. (23b)

$$\sigma_{xx} = -\rho g d \left(\frac{1 + (1 - 2\lambda_{HR}) \sin \phi}{1 - \sin \phi} \right) - \rho_w g (h_1 - h_2). \quad (24)$$

The force corresponding to the landward horizontal stresses in the sedimentary overburden (Eqn. 4) when hydrostatic pore fluid pressure is taken into account becomes

$$F'_1 = - \int_{h_c}^{h_c+h_1} \sigma_{xx, \text{extension}} dz = \frac{1}{2} \rho g h_1^2 k_w \quad (25)$$

and the force, F''_2 , (Eqn. 5) becomes

$$F''_2 = \int_{h_c}^{h_c+h_2} \sigma_{xx, \text{contraction}} dz = -\frac{1}{2} \rho g h_2^2 k'_w - \rho_w g (h_1 - h_2) h_2 \quad (26)$$

The force balance equation for a system with yielding sedimentary overburden is thus

$$F'_1 + F''_2 + F'_p + F_c + F_w = 0 \quad (27)$$

which when inserting Eqns (25), (26), (14), (9) and (15) results in

$$\rho g h_1^2 k_w - \rho g h_2^2 k'_w - 2\rho_w g (h_1 - h_2) h_2 + h_c (\rho - \rho_w) g (h_1 - h_2) - 2\eta \frac{V_c}{h_c} (x_2 - x_1) - \rho_w g (h_1 - h_2)^2 = 0. \quad (28)$$

Using the scaling force, $F_s = \rho g h_c^2$ to nondimensionalise, the force balance equation gives, in the case of water loading

$$(h_1^*)^2 k_w - (h_2^*)^2 k'_w - 2\rho_w^* (h_1^* - h_2^*) h_2^* + (1 - \rho_w^*) (h_1^* - h_2^*) - \rho_w^* (h_1^* - h_2^*)^2 - 2V_c^* l^* = 0 \quad (29)$$

where the nondimensional parameters are

$$h_1^* = h_1/h_c, \quad h_2^* = h_2/h_c, \quad \rho_w^* = \rho_w/\rho, \quad l^* = (x_2 - x_1)/h_c \quad \text{and} \quad V_c^* = V_c/V_s, \quad \text{where } V_s \text{ is the scaling velocity, } V_s = \rho g h_c^2/\eta.$$

In the special case of hydrostatic pore pressure this reduces to

$$\left[(h_1^*)^2 k - (h_2^*)^2 k^{-1} + h_1^* - h_2^* \right] (1 - \lambda_{HR}) - 2V_c^* l^* = 0 \quad (30)$$

which is the same as that for the dry system, Case 1 (Eqn. (11)), except for the term containing the pore pressure ratio. This simplification occurs because the effective stress in the sediment is everywhere reduced by an amount equal to hydrostatic fluid pressure acting in the sediment alone. The overlying water has no additional effect on the overburden but the differential pressure driving the Poiseuille flow in the salt is reduced. The horizontal buttress force disappears because it is balanced by the hydrostatic fluid pressure in the sediment.

Depending on the circumstances, taking into account the effects of pore pressures in the sediments using the Hubbert–Rubey pore pressure ratio may provide a more accurate representation of the sediment properties in systems submerged under water than a method based on $\lambda = p_f/p$ (Eqn. (12)). In open systems where the pore fluid pressures are directly connected to the surface and not confined, the pore fluid pressure will be close to hydrostatic and is best approximated by $p_f = \lambda_{HR} \times \sigma_z$, where λ_{HR} takes the hydrostatic values. However, in a closed system pore fluids will experience pressures that are proportional to p (the solid pressure) and, therefore, the alternative definition of λ is more appropriate, such that $p_f = \lambda \times p$. In this circumstance the fluids have no sense of the weight of the overburden, σ_z . Both approaches are, at best, approximations to the pore fluid pressures. Overpressures are commonly observed and attributed to compaction disequilibrium, hydrocarbon generation,

diagenetic reactions and flow focusing along faults (Hart *et al.*, 1995; Dugan & Flemings, 2000; Flemings *et al.*, 2002; Lupa *et al.*, 2002; Mourgues & Cobbold, 2003; Vendeville & Gaullier, 2003). Each of these requires a particular calculation of the associated fluid pressures, which is beyond the scope of this paper. Here, we will focus on the simple, but equally important case where pore fluid pressures are hydrostatic and we will use $p_f = \lambda_{HR} \times \sigma_z$.

Subaerial versus submarine systems

The force balance equations (Eqns (11), (18) and (29)) define the horizontal overburden velocities when the sediments are on yield in the initial configuration. By considering the case where the velocity, V_c^* , is zero, these equations can be used to estimate the situation where the system is on the verge of failure and F_1 and F_2 attain their limiting values. Figure 4a shows this failure limit for the specific case where the landward overburden thickness is constant ($h_1^* = 4.5$), which, for instance, corresponds to a system with a 1000 m thick salt layer overlain by 4500-m sediments in the landward region. For increasing overburden strength (here expressed by the increasing values of the internal angle of friction, ϕ) the thickness, h_2^* , at the failure limit decreases. A comparison of the failure limits for Case 1 with and without water loading (Fig. 4a) emphasises that the water load has a significant stabilising effect on the system. As expected from Eqns (11) and (30) the failure limit for Case 2 at hydrostatic pore pressure and Case 1 without water loading coincide. This is because the hydrostatic fluid pressure, when $V_c = 0$, affects all the terms in the force balance equally (Eqn. (30)). Therefore for a given internal angle of friction, ϕ , failure will occur for the same overburden thickness, h_2^* , for both cases. It should be emphasised however, that the failure limits will not be the same for systems with nonhydrostatic pore pressures (Eqn. (29)).

The effect of using the Hubbert–Rubey fluid pressure ratio in Case 2 is illustrated in Fig. 4b which shows the failure limit as a function of the pore pressure ratio, λ_{HR} . The internal angle of friction is, $\phi = 30^\circ$ and the density ratio between the water and the overburden is $\rho_w^* = 1/2.3$. A decrease in the pore pressure ratio increases the overburden strength, and reduces the values of h_2^* at the limit of overburden failure. Case 1 without water loading, is significantly more unstable than the same model with water loading, illustrating that the buttress force, the reduced Poiseuille flow and the increased seaward overburden strength caused by the water significantly affect the system. The result (Fig. 4b) also shows that there is a significant difference in the failure limit between Case 1 with water loading and λ and ϕ_{eff} defined by Eqn. (12) and Case 2 with $\lambda = \lambda_{HR}$.

Examples of the variation of Couette velocity with seaward overburden thickness, h_2^* , are shown in Fig. 5. The velocities are for systems with constant transition zone width, $l^* = 400$, and landward overburden thickness, $h_1^* = 4.5$. For Case 1, velocities are shown with and without water loading. In addition, velocities are shown for a system with dry-sand rheology ($\phi_{eff} = 30^\circ$) and for a system

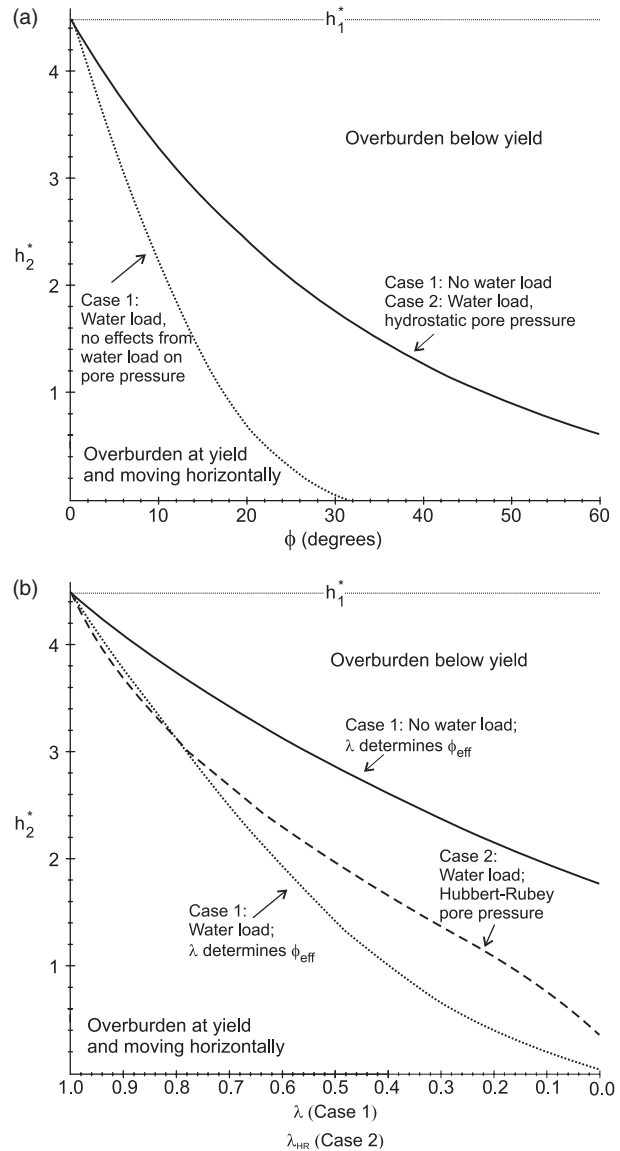


Fig. 4. Failure limit of overburden. (a) Failure limit as a function of the internal angle of friction, ϕ , and seaward overburden thickness, h_2^* , for $h_1^* = 4.5$. Solid line: Case 1 without water loading and Case 2 (water loading and hydrostatic pore pressure in the frictional–plastic overburden). Dotted line: Case 1 with water loading. (b) Failure limit as a function of the pore pressure ratio. Internal angle of friction, $\phi = 30^\circ$. Solid line: Case 1 without water loading (the pore pressure ratio λ determines the effective angle of friction, ϕ_{eff}). Dotted line: Case 1 with water loading (the pore pressure ratio λ determines the effective angle of friction, ϕ_{eff}). Dashed line: Case 2. Hubbert–Rubey pore pressure ratio, λ_{HR} , is used.

in which the effective internal angle of friction approximates sediments under hydrostatic pore pressure (Eqn. (12)) ($\phi_{eff} = 16.42^\circ$; density, $\rho = 2300 \text{ kg m}^{-3}$). The velocities decrease for increasing values of h_2^* , and for large values of h_2^* the overburden is below yield and the overburden velocity is zero. The velocities are lower for dry sediments (Case 1; $\phi_{eff} = 30^\circ$) than for wet sediments (Case 1; $\phi_{eff} = 16.42^\circ$). In addition, the water load significantly decreases the overburden velocities and for the system considered here,

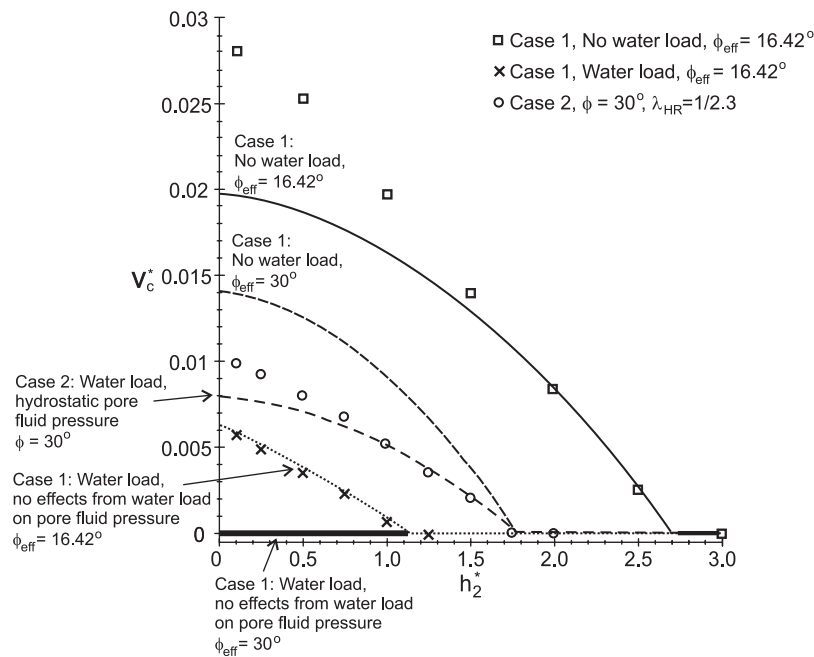


Fig. 5. Initial velocities of the overburden transition zone for varying overburden thickness, h_2^* . $l^* = 400$, $h_1^* = 4.5$. Solid line: Case 1 without water loading, $\phi_{\text{eff}} = 16.42^\circ$. Dashed line: Case 1 without water loading, $\phi_{\text{eff}} = 30^\circ$. Dotted line: Case 1 with water loading, $\phi_{\text{eff}} = 16.42^\circ$. Thick solid line: Case 1 with water loading, $\phi_{\text{eff}} = 30^\circ$. Squares, crosses and circles: corresponding initial overburden velocities predicted by the numerical model.

a model with water load and $\phi_{\text{eff}} = 30^\circ$ will have sediments below the yield limit even for small values of h_2^* and will be characterised entirely by Poiseuille flow.

The difference between the two definitions of the pore fluid pressure may be assessed by comparing the velocities for Case 2 with the velocities for the Case 1 model with water load and wet sediments ($\phi_{\text{eff}} = 16.42^\circ$). The faster velocities for Case 2 occur because the solid pressure (mean stress) deviates from the weight of the overburden. This analysis shows that water load and pore fluid pressures have significant effects on passive margin salt–sediment systems. In the following we present finite-element experiments, which include water loading and hydrostatic pore fluid pressures. We use $p_f = \lambda_{\text{HR}} \times \sigma_z$, which is the most appropriate choice of the definition of λ when the system is open and pore fluid pressures are hydrostatic.

NUMERICAL MODEL

We use a 2D plane-strain finite-element model to investigate the evolution of the salt tectonic systems. The model is a velocity based viscous–plastic model (Fallsack, 1995; Willett, 1999) that is designed for large deformation fluid Stokes flows and solves the equations for conservation of momentum and mass. The model uses an Arbitrary Lagrangian–Eulerian (ALE) method in which computations are made on an Eulerian grid that adapts to the evolving model domain. The material properties are tracked and updated using a set of Lagrangian nodal points. This approach allows calculations to be made for large strains. Water loading is included as a boundary load, which increases the solid and fluid pressures of material in the

model according to the overlying water column. We use linear viscosity to represent viscous salt

$$\sigma' = 2\eta\dot{\epsilon} \tag{31}$$

where σ' , is the deviatoric part of the stress tensor, η is viscosity and $\dot{\epsilon}$ is the strain rate. Plasticity is modelled by the Drucker–Prager yield criterion, which is equivalent to the Mohr–Coulomb criterion for incompressible, plane-strain deformation

$$(\mathcal{J}'_2)^{1/2} = p \sin \phi \tag{32}$$

where \mathcal{J}'_2 is the second invariant of the deviatoric stress and p is the solid pressure. No sediment compaction is considered.

In this study we consider a 1000-m thick viscous salt substratum (h_c) that is overlain by a frictional–plastic overburden wedge of laterally varying thickness. The total model thickness, h , varies from h_1+h_c to h_2+h_c following the half-Gaussian function

$$h(x) = h_c + \begin{cases} h_1 & \text{if } x < x_1 \\ h_2 + (h_1 - h_2) \exp\left(-\frac{(x-x_1)^2}{b^2}\right) & \text{if } x \geq x_1 \end{cases} \tag{33}$$

where h_1 and h_2 are the landward and seaward limiting overburden thicknesses. This smooth surface is used to avoid potential numerical effects related to abrupt changes in sediment geometry and to approximate the gradual change in sediment thickness observed in nature. The width of the transition region (Fig. 6), l , is determined by the value

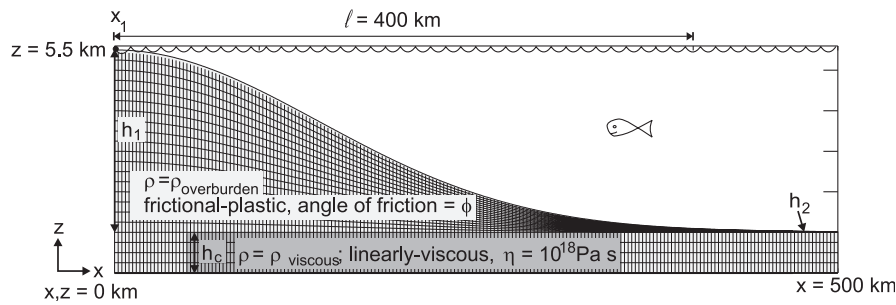


Fig. 6. Numerical model set-up. The model domain is 500 km long. The salt layer is 1000 m thick and the overburden thickness varies from h_1 to h_2 over a length, $l \sim 2d$. Light grey region: Frictional-plastic sediment material, density $\rho_{\text{overburden}} = 2300 \text{ kg m}^{-3}$, internal angle of friction ϕ . Medium grey region: linearly-viscous material, density $\rho_{\text{viscous}} = 2200 \text{ kg m}^{-3}$, viscosity $\eta = 10^{18} \text{ Pa s}$. Fish indicates overlying water column. Vertical exaggeration = 28.

of $w = 200 \text{ km}$ (l approximately equals $2w$) and the transition starts at $x = x_1$.

The Eulerian and Lagrangian grids consist of 88 vertical by 800 horizontal elements that are adjusted vertically to form the Gaussian-shaped topography (Fig. 6). The upper model surface is loaded in the normal direction by the weight of the current water column. All other boundaries have zero velocity parallel and perpendicular to the boundaries. The density difference between the overburden and the salt layer is -100 kg m^{-3} ($\rho_{\text{sediment}} = 2300 \text{ kg m}^{-3}$, $\rho_{\text{salt}} = 2200 \text{ kg m}^{-3}$) and the salt viscosity is constant at 10^{18} Pa s . For simplicity, the water level is kept constant at 5500 m ($h_1 + h_c$) in all models and a water density of $\rho_w = 1000 \text{ kg m}^{-3}$ is used.

COMPARISON OF ANALYTICAL AND NUMERICAL OVERBURDEN VELOCITIES

To compare the numerical model with the analytical theory, we analyse the calculated overburden velocities at the earliest timesteps (before any significant change in model geometry has occurred) for a set of numerical models. In these models the salt layer is much wider (1000 km) than the overburden transition zone (400 km; the width l shown in Fig. 6) to prevent the predicted velocities from being affected by the finite width of the salt layer. Models were run using the water loading cases described in the failure analysis section and with varying seaward overburden thickness, h_2^* . The calculated initial overburden velocities (Fig. 5) agree with the analytical predictions for larger values of h_2^* , that is, when the overburden is below yield or at yield, but close to the yield limit. For small seaward overburden thicknesses, the deviation between the analytical and numerical results may be due to inaccuracy in the simplified horizontal force balance from the thin-sheet approximation assumed in the analytical theory.

DYNAMICAL MODELS OF SEDIMENT PROGRADATION OVER SALT

Model set-up

In this section we investigate the deformation resulting from sediment progradation above salt. The total model

length is 500 km, the salt layer is 300 km wide and 1 km thick, and w is 200 km, which results in an upper bound estimate of the width of the overburden transition zone that is about 400 km (Fig. 6), but most of the transition occurs in a 300 km wide zone. The width of the transition zone is at the upper end of what has been observed on typical passive continental margins (Demercian *et al.*, 1993; Tari *et al.*, 2002), which range from 200–450 km offshore Brazil (Demercian *et al.*, 1993; Cobbold *et al.*, 2001b), through approximately 250 km in the US Gulf of Mexico (Peel *et al.*, 1995; Trudgill *et al.*, 1999) to 100–200 km on many west African margins and offshore Nova Scotia (Wade & MacLean, 1990; Tari *et al.*, 2002). Zones of deformable material with the same properties as the overburden are included at the landward and seaward ends of the model. These zones represent regions beyond the limits of the salt deposition and also act as buffer zones that are sufficiently wide to prevent effects from the lateral model boundaries. Other model properties are the same as those described in the Numerical Model section.

Six models are investigated. Model 1 shows the evolution of a simple system with constant rate of sediment progradation. The effects of water loading and hydrostatic pore pressure ($\lambda_{\text{HR}} = 1/2.3$, Case 2 in the failure analysis section) are included and the internal angle of friction of the overburden is $\phi = 30^\circ$. Model 2 is the same as Model 1 except water loading and pore pressure effects are omitted. We then investigate how sediment properties (strain softening; Model 3) and sedimentation patterns of increasing complexity (Models 4–6) can affect the Model 1 system.

Sediment progradation above salt (Model 1)

The evolution of a system where sediments prograde over salt (Model 1) is illustrated in Fig. 7. Initially, the sediment transition zone is landward of the salt basin (x_1 in Eqn. (33) is -350 km), and the sedimentary overburden is $h_2 = 10 \text{ m}$ thick above most of the salt layer (Fig. 7a). Sediment progradation is modelled by translating the sediment profile function (Eqn. (33)) from landward to seaward at the progradation velocity, $V_{\text{sp}} = 0.5 \text{ cm yr}^{-1}$. New overburden material that fills the region between the current model surface and the prograding surface is added to the model calculations. Where the current model surface is above

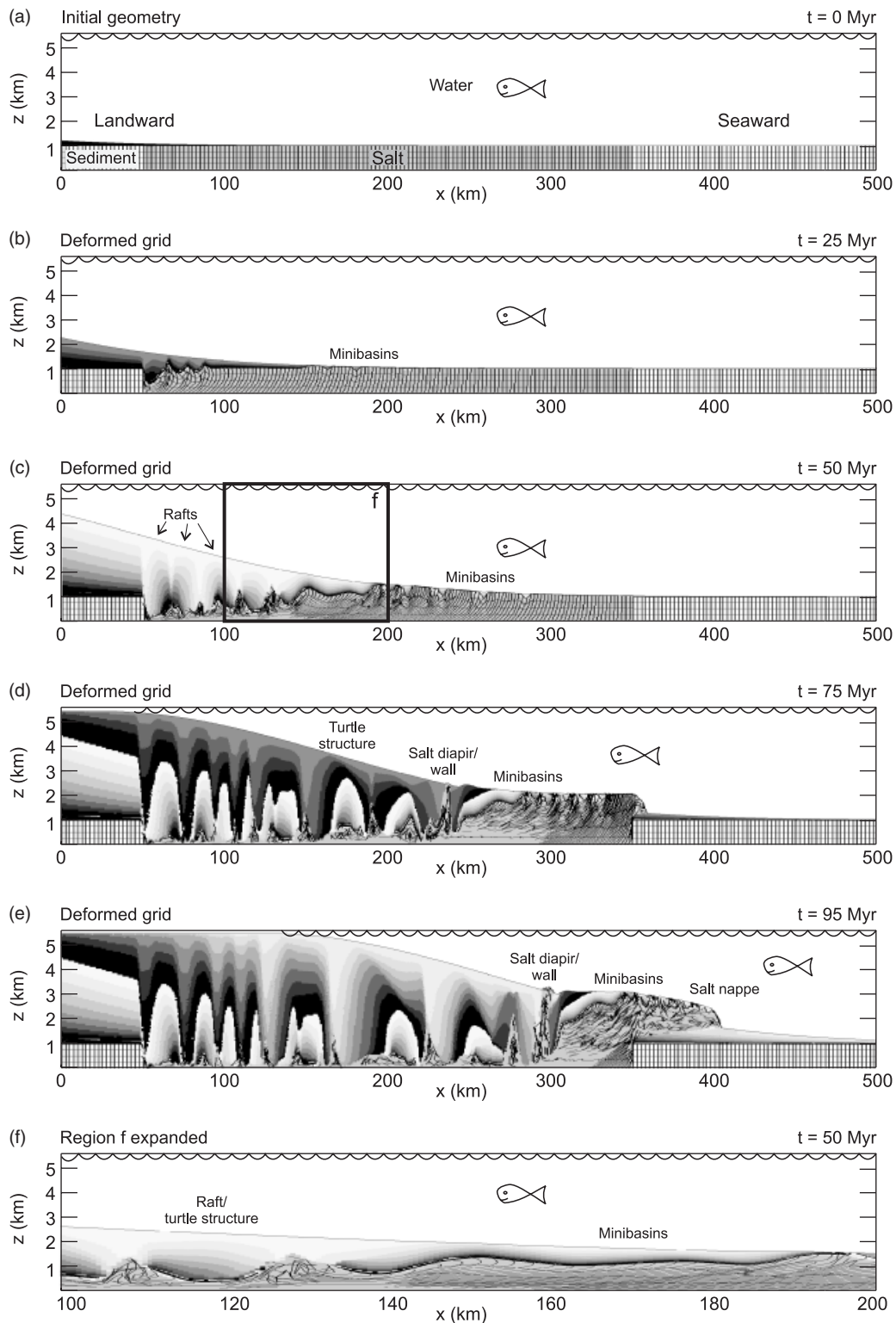


Fig. 7. Model 1. Dynamical model of sediment progradation above salt. Sediment progradation rate, $V_{sp} = 0.5 \text{ cm yr}^{-1}$. Salt is medium grey. Sedimentary overburden is light grey. Deposited sediment is dark to light grey. Each colour corresponds to deposition during 5 Myr. (a) Model set-up. Each cell on the figure corresponds to 4×4 elements in the Lagrangian grid. (b) Model after 25 Myr. (c) Model after 50 Myr. (d) Model after 75 Myr. (e) Model after 95 Myr. Vertical exaggeration in (a–e) = 15. (f) Close-up of minibasins after 50 Myr. Vertical exaggeration = 3 (for link to colour animation, see end of paper).

the prograding profile, material is neither added nor removed. The sediment material that is added during progradation has the same properties as the pre-existing sediment, and the greyscales (Fig. 7) represent the strati-

graphic layering. The water load is adjusted for the current configuration of the sediment profile.

As the sediment wedge progrades onto the salt, the differential sediment load initiates a combined Poiseuille and

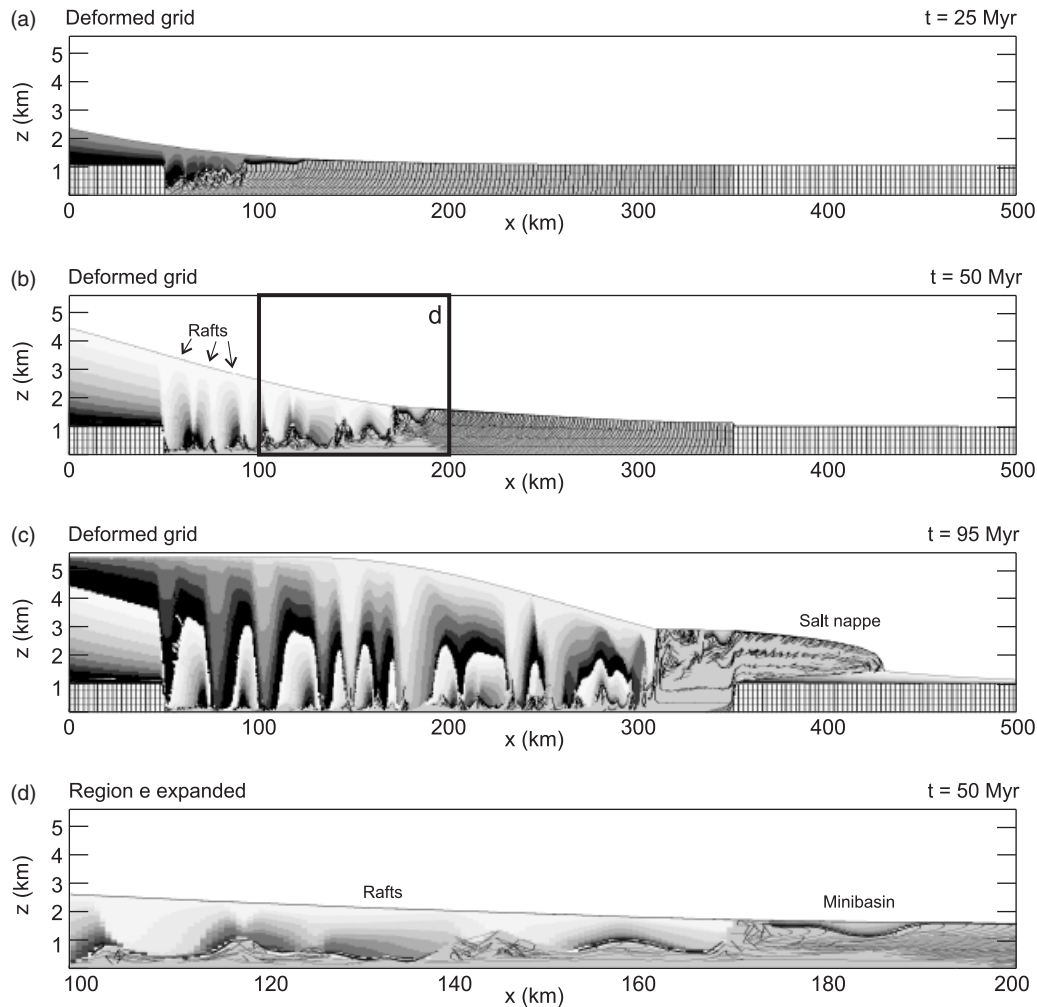


Fig. 8. Model 2. Same as Model 1 (Fig. 7) but no water loading or pore fluid pressures included. Effective internal angle of friction $\phi = 30^\circ$. (a) Model at 25 Myr. (b) Model at 50 Myr. (c) Model at 95 Myr. Vertical exaggeration in a–c = 15. (d) Close-up of rafts at 50 Myr. Vertical exaggeration = 3 (for link to colour animation, see end of paper).

Couette seaward salt flow, which deforms the distal part of the sediment wedge and initiates depocentres that evolve into minibasins (Fig. 7b, $x = 150\text{--}200$ km). The salt beneath the minibasins is evacuated whereby accommodation space is continuously created allowing the minibasins to grow. The evacuated salt accumulates and initiates diapirs that separate the minibasins. Sediment progradation causes the region of overburden shortening to move seaward and the minibasins to get progressively younger in the seaward direction. At 50 Myr (Fig. 7c) the region of shortening has progressed to $x = 300$ km. Landward of this contractional region, the sediments fail by extension as a consequence of the differential sediment load (Fig. 7f) and the viscous flow is dominated by Couette flow (*cf.* Fig. 2). Extension is localised above the pre-existing salt diapirs where the system is weakest. Continued sediment filling of the extensional depocentres, however, prevents the development of local differential pressures and, therefore, inhibits salt diapirism in the extending regions. The diapirism that does occur in these regions is driven by buoyancy of the salt. The minibasins that formed during the

earlier model stages now become part of the rafts that are located between the necking regions and are inverted to form turtle structures (Fig. 7f).

At 75 Myr (Fig. 7d) the salt flow has reached its seaward autochthonous limit and a salt nappe has started to form. The net horizontal and vertical flux of salt and sediment is greater than the sediment progradation rate and beyond $x = 250$ km (Fig. 7d) the distal material moves, shortens and thickens ahead of the kinematically specified sediment profile, which descends below the sediment surface landward of the small surface topographic bump. Owing to our choice of sedimentation model, this seaward part of the sediment surface no longer receives additional sediment and consequently no new minibasins are formed in this region. Instead, the existing minibasins are carried passively on top of the advancing system. Uplift of the sediment surface above the sedimentation profile also allows surface irregularities to develop and the associated local differential pressures enhance the buoyancy driven salt diapirism, and a salt diapir has started to pierce the overburden ($x = 235$ km).

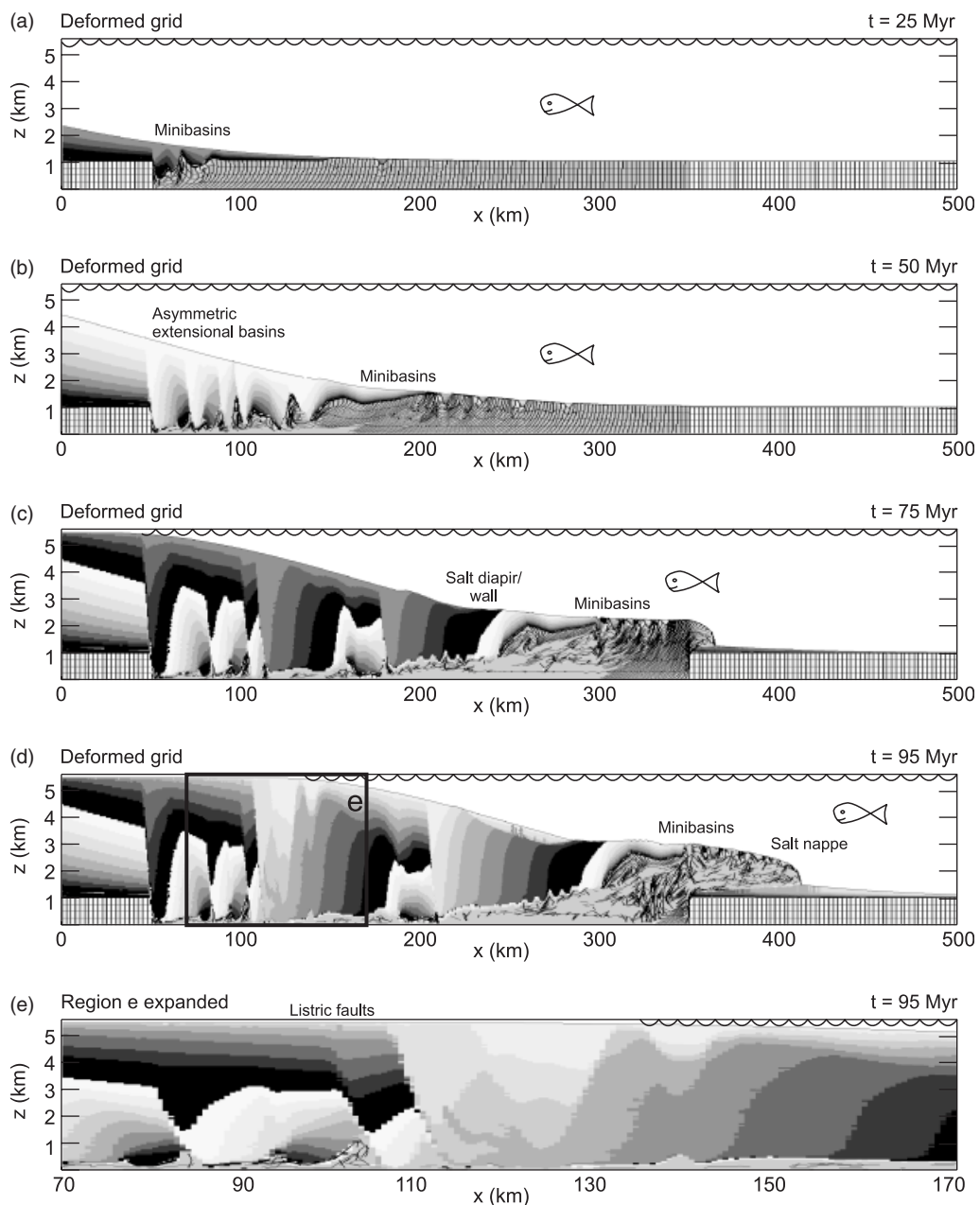


Fig. 9. Model 3. Strain softening of the sedimentary overburden. Model set-up is the same as for Model 1 (Fig. 7) except that the internal angle of friction, ϕ , of the sediments is reduced from 30° to 10° as the strain increases from 0.5 to 1. Salt is medium grey. Sedimentary overburden is light grey. Deposited sediment is dark to light grey. Each colour corresponds to deposition during 5 Myr. (a) Model after 25 Myr. (b) Model after 50 Myr. (c) Model after 75 Myr. (d) Model after 95 Myr. Vertical exaggeration in (a–e) = 15. (e) Close-up of asymmetric extensional basins after 95 Myr. Vertical exaggeration = 3 (for link to colour animation, see end of paper).

After 95 Myr (Fig. 7e) the salt nappe has advanced 50 km beyond the autochthonous limit of the salt and is still above the prograding sedimentary wedge. However, the kinematically prograding sediments have started to overtake the salt nappe at its seaward end ($x = 400$ km) forcing the salt nappe to climb up the stratigraphy section. This distal sedimentation may eventually lead to reduced flow velocities and burial of the salt nappe. The salt diapir that had formed by 75 Myr has been carried with the overburden about 60 km seaward. It is bounded by two asymmetric normal growth shear zones, which develop because the

weak salt localises deformation along the sediment-salt diapir interface.

Subaerial versus submarine systems (Model 2)

The importance of water loading and pore pressure effects may be assessed by comparing a model where no water loading or pore pressure effects are included (Model 2; Fig. 8) with Model 1 (Fig. 7). In Model 2 the internal angle of friction of the sediments is, $\phi = 30^\circ$, which approxi-

mates dry sand. Although the overburden is stronger, the lack of water load leads to overburden velocities that are about twice as high as those for Model 1 (Fig. 5). This leads to a more significant component of Couette flow already at early model stages (25 Myr; Fig. 8a) and early extensional failure of the relatively thin overburden, which causes inversion of the minibasins and shorter landward rafts between the extensional basins (Fig. 8b, d).

The higher velocities also lead to more efficient salt evacuation, suppress salt diapirism beneath the shelf (Fig. 8c) and cause the salt to flow further ahead of the prograding sediment wedge. At 95 Myr the salt nappe has moved about 30 km further seaward than for Model 1. Only one minibasin exists on top of the salt nappe, because most of the minibasins that formed during the early stages were inverted and became part of the extensional system. This shows that although the first-order pattern of landward extension and seaward contraction also characterise a dry-system model, the formation and evolution of secondary structures, such as minibasins, are sensitive to the overburden velocities and thereby to the effects of water load and pore fluid pressures.

Strain softening of the overburden (Model 3)

Deformation may lead to weakening of the frictional sediments due to, for instance, grain size reduction, fault and fracture development (Kirby, 1985), and increase in pore fluid pressure (e.g. Flemings *et al.*, 2002; Lupa *et al.*, 2002). In this section, the effects of strain softening are investigated through a model in which the internal angle of friction, ϕ , of the sediment is reduced linearly from 30° to 10° as the local strain, measured by the second invariant, increases from 0.5 to 1 (Model 3; Fig. 9). All other model parameters are the same as for the Model 1 (Fig. 7), including the hydrostatic pore fluid pressure in the sediments.

During the early model stages, the effects of strain softening are minor because the strain of the sediment is small. At 25 Myr (Fig. 9a) the main difference between Models 1 and 3 is that only two minibasins have developed in the model with strain softening, whereas three basins had formed in the model without strain softening. This result illustrates the tendency for the deformation localised by strain softening to persist at a particular location, at the expense of the development of new deformation zones (minibasins in this case). The localisation effects of strain softening are more significant during the subsequent extensional failure of the landward region, which is localised along seaward dipping listric shears and leads to the development of asymmetric depocentres (i.e. half grabens) in the landward region (Fig. 9b, c). Strain softening leads to fewer extensional basins. At 95 Myr (Fig. 9d, e) only two listric shears characterise the region $x = 120\text{--}300$ km by comparison with 4 in Model 1. This persistence of active strain-softened listric shears leads to the primary difference between Models 1 and 3 in which ~ 80 km wide regions of sediment accumulation and rollover develop in Model 3 in the hanging wall of the two longest lived listric normal faults (at 110

and 210 km, Fig. 9d, e) as these regions are transported seaward on top of the mobile salt. Natural equivalents of this type of sedimentary structure could be misinterpreted to imply sediment progradation from seaward to landward and not the progressive wholesale seaward translation of the hanging wall as a component of the unstable flow of overburden above the salt.

In the seaward region, the difference between Models 1 and 3 is less remarkable because the system is dominated by the salt which does not strain soften in either model. Strain softening leads to overall weaker overburden, which results in somewhat larger velocities than for Model 1. However, the overall development of the system has led to a similar size salt nappe to that of Model 1 (*cf.* Figs 9c, d and 7d, e). This result indicates that the strain softening does not increase the post-yield velocity of the overburden significantly and, therefore, that the Couette viscous drag (Eqs (28) and (29)) exerts a strong control on the velocity of the system. For lower salt viscosities the velocities would be more sensitive to the strain softening. At 95 Myr (Fig. 9d) the minibasins on top of the salt nappe have been translated passively with the salt nappe indicating that this part of the system is also insensitive to strain softening of the overburden while it is not receiving sediment (*cf.* Figs 9d and 7e).

Transition from sediment progradation to sediment starvation (Model 4)

The models investigated so far assume a constant sediment progradation rate ($V_{sp} = 0.5 \text{ cm yr}^{-1}$). However, in nature the sedimentation rate often varies, for instance, owing to climate variations or variations in sediment source area or sediment transport direction. In this section we investigate the effects of a period of sediment starvation. Model 4 (Fig. 10) has the same initial model set-up as Model 1 (Fig. 7) and sediments prograde into the system at a sediment progradation rate $V_{sp} = 0.5 \text{ cm yr}^{-1}$ during the first 50 Myr. At 50 Myr, sedimentation ceases and the system continues to evolve as a consequence of the instability caused by the existing model geometry.

Only 5 Myr after sedimentation has terminated (55 Myr; Fig. 10b) the effect of sediment starvation is remarkable. In the landward section, faulting and sediment thinning owing to extension result in the development of troughs at the sediment/water interface. This bathymetric variation causes local differential pressures at the level of the salt forcing it to flow upward into the necking low-pressure regions and salt diapirs/walls to develop. The diapirism is certainly aided by the buoyancy of the salt but the local differential pressure is essential for diapirs to reach the sediment surface as can be demonstrated by comparison with Model 1 where the diapirs do not reach the surface.

Salt diapirism is most significant in the region $x = 100\text{--}150$ km where the salt layer is still relatively thick and the Couette velocities and extension rates are fastest. Landward of this region, less salt is available to form diapirs and the thinner salt channel results in smaller velocities and less extension. Seaward of the extending region

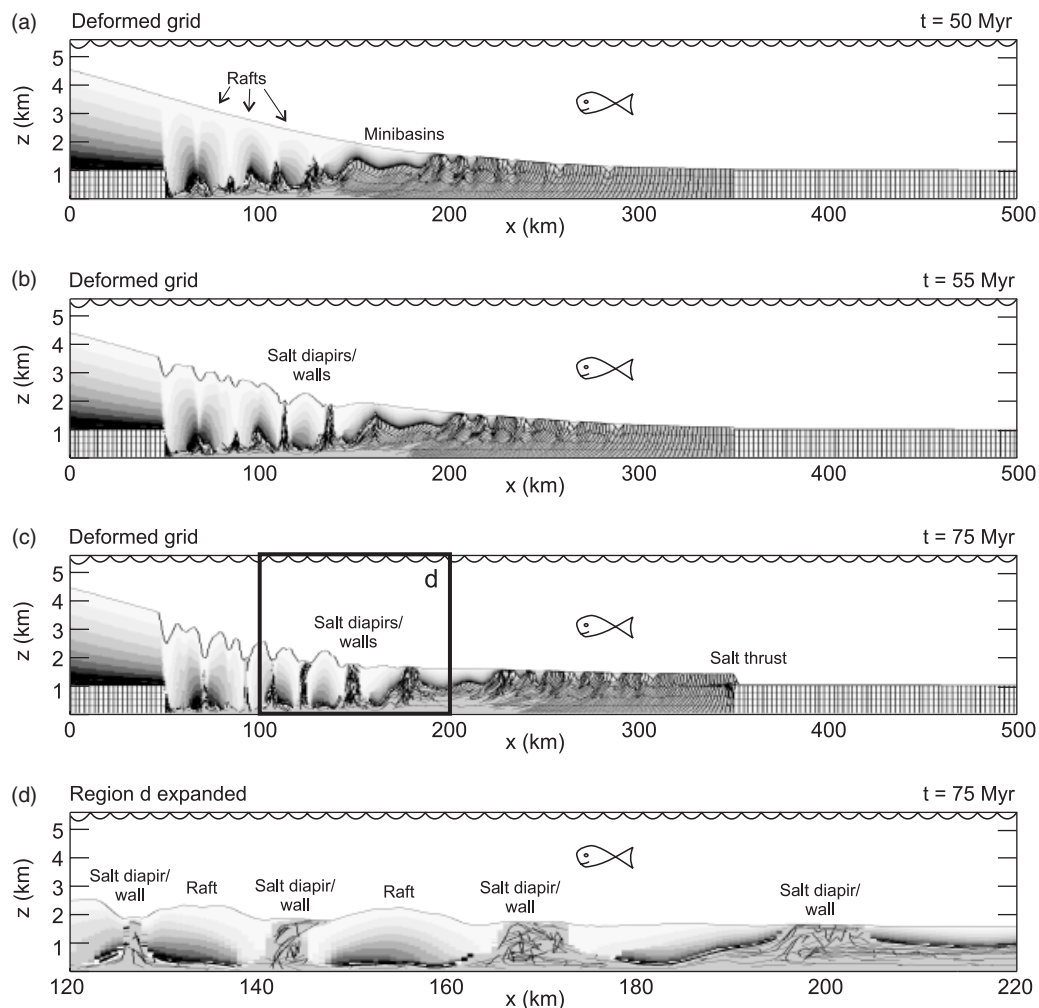


Fig 10. Model 4. Sediment starvation. Same as Model 1 (Fig. 7) except that sedimentation terminates at 50 Myr. Salt is medium grey. Sedimentary overburden is light grey. Deposited sediment is dark to light grey. Each colour corresponds to deposition during 5 Myr. Each cell on the figure corresponds to 4×4 elements in the Lagrangian grid. (a) Model at 50 Myr (just before sedimentation terminates). (b) Model at 55 Myr (5 Myr after sedimentation has terminated). (c) Model at 75 Myr. Vertical exaggeration in (a–c) = 15. (d) Close-up of salt diapirs and sediment rafts after 75 Myr. Vertical exaggeration = 3 (for link to colour animation, see end of paper).

($x > 200$ km) the system is less affected at this stage by the termination of sedimentation. The minibasins that had already formed in this region, are passively translated seaward on top of the salt without any significant internal deformation, demonstrating that additional sedimentation is required if the minibasins are to grow.

At 75 Myr, 25 Myr after sedimentation has terminated (Fig. 10c) landward extension has caused significant sediment thinning, most of the salt has been evacuated and several diapirs now penetrate the sedimentary overburden. The continued seaward salt evacuation results in a salt thrust at the seaward depositional limit of the salt. The salt level is close to constant at 1.5 km across the model, which indicates that it is approaching its gravitational equilibrium. A comparison of Models 1 and 4 (Figs 7d and 10c) at 75 Myr shows that the reduced sediment input in Model 4, as expected, results in less salt evacuation and a less developed salt nappe. There is also a corresponding distinct difference in the gravitationally adjusted surface level of the distal evacuated salt between Models 1 and 4. Clearly,

the salt has been pumped to a higher level by the continued sediment progradation in Model 1.

Transition from sediment progradation to aggradation (Model 5)

Although complete termination of sedimentation may occur in nature, a more likely process is, for instance, a transition from an environment dominated by sediment progradation to a setting with lower sediment input from the onshore regions, sediment bypass of the shelf and upper slope and an aggradational pattern on the lower slope and rise. In Model 5 (Fig. 11) we investigate the effects of such a transition. During the first 50 Myr, this model is the same as Model 1 (Fig. 7) and sediments prograde into the system at a progradation rate, $V_{sp} = 0.5 \text{ cm yr}^{-1}$. At 50 Myr the height of the sediment profile (h_1) is reduced to 2500 m, the width of the overburden transition zone is increased to $l = 600$ km ($w = 300$ km, Eqn. (33)) and x_1 is reset to -400 km. This creates a new sediment profile that is lower and wider than the

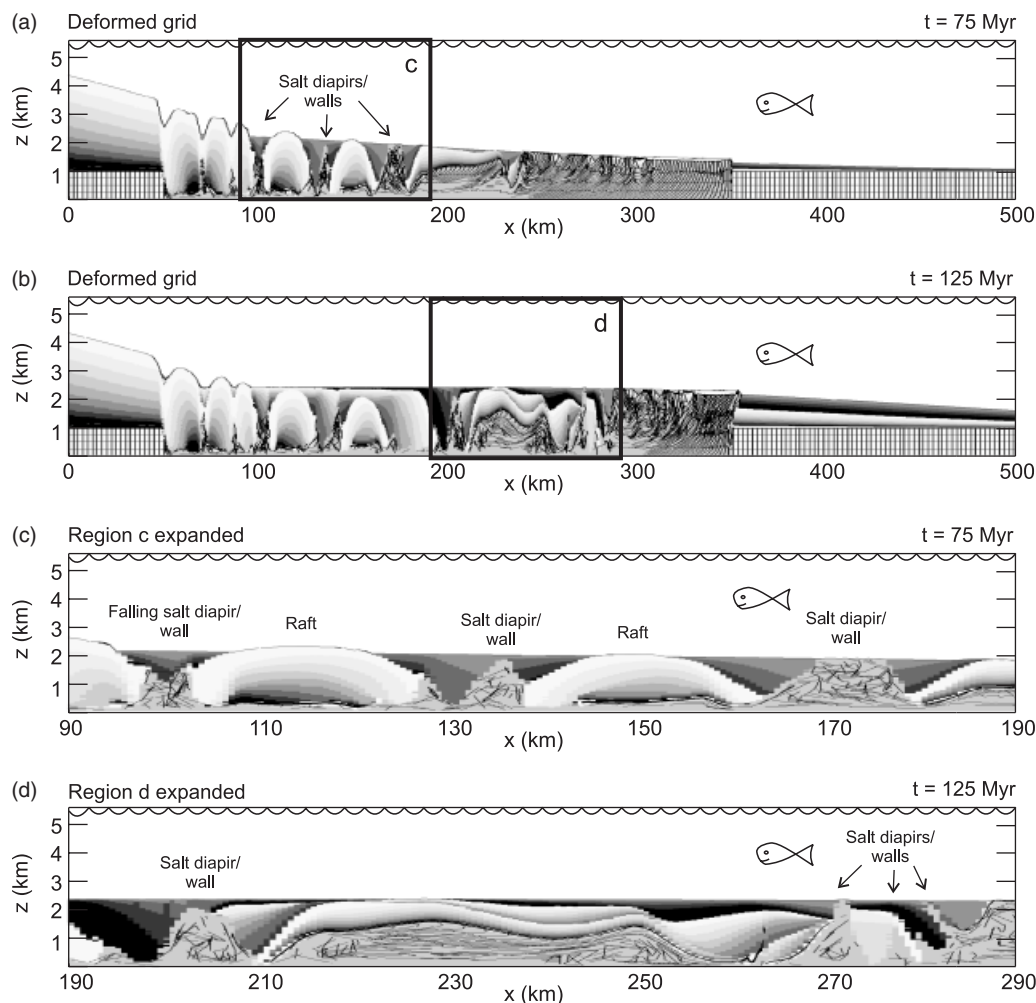


Fig 11. Model 5. Sediment aggradation. Same as Model 1 (Fig. 7) except that sedimentation changes from progradation to aggradation at 50 Myr. Salt is medium grey. Sedimentary overburden is light grey. Deposited sediment is dark to light grey. Each colour corresponds to deposition during 5 Myr. Each cell on the figure corresponds to 4×4 elements in the Lagrangian grid. (a) Model at 75 Myr (25 Myr after sedimentation pattern has changed). (b) Model at 125 Myr. Vertical exaggeration in (a) and (b) = 15. (c) Close-up of salt walls and sediment rafts after 75 Myr. (d) Close-up of distal diapirs after 125 Myr. Vertical exaggeration in (c) and (d) = 3 (for link to colour animation, see end of paper).

initial one and results in no sedimentation on the existing shelf and most of the slope. The lower slope and more seaward parts of the model experience sedimentation that has a more aggradational character, owing to the wider sediment transition zone. The sediment progradation rate, V_{sp} , remains constant at 0.5 cm yr^{-1} .

This model also responds quickly to the change in sedimentation pattern and develops local differential pressures and salt diapirs in the landward region. The salt diapirs grow passively with the aggrading sedimentation, and at 75 Myr this has led to well-developed proximal salt diapirs ($x = 100, 130, 170$ km; Fig. 11a, c). The diapirs are best developed in the seaward direction (Fig. 11c) because the salt supply is limited at the landward end of the profile where significant amounts of salt were already evacuated during the first progradation phase (0–50 Myr) (Fig. 11a). Furthermore, the sedimentation rates increase toward the landward region ($x = 100$ – 150 km) where they eventually exceed the rate at which the salt can rise and the diapirs begin to become buried (Fig. 11c). At the distal end of the

model, the aggrading sedimentation style prevents the salt from overthrusting its depositional limit, partly because the subhorizontal sediment surface produces only a small regional differential sediment load, which diminishes the overall seaward salt evacuation.

At 125 Myr, the landward diapirs have all been buried beneath the aggrading sediment, because the sedimentation rates exceed the rate of diapirism owing to the paucity of salt supply and the near horizontal sediment surface (Fig. 11b, d) which results in limited differential pressures in the salt. No further movements occur in this region even though the salt is buoyant. Seaward progradation of the sediment transition zone causes the distal diapirs to grow passively with the aggrading sediments. At the seaward autochthonous salt limit, a massive block of salt has accumulated because distal sedimentation prevents further lateral flow. Further progradation of the sediment profile would also reduce the differential pressures in this region, and eventually this massive salt structure will stop growing and become buried beneath the aggrading sediment.

Sediment bypass (Model 6)

The previous models specified complete sedimentation up to a prescribed profile level. Where these profiles produce smoothly varying bathymetry local pressure gradients did not develop even though the underlying overburden may have been unstable and was extending (e.g. Model 1; Fig. 7c, d). Hence, it is only when this kinematically specified sedimentation terminates or the sediment progradation profile is changed (Models 4 and 5) that extension can create local bathymetric variations (basins) and the consequent local pressure variations will

force salt diapirism. In nature, these basins may only be partially filled by sediment as a consequence of the plan-form routing of sediment dispersal systems (e.g. out of plane sediment transport, in which sediment bypasses the basins through strike incised channel/levee complexes (flow bypass; Sinclair & Tomasso, 2002) or fine-grained material in suspension escaping the basins (flow stripping; Sinclair & Tomasso, 2002). Such processes are simulated in Model 6 (Fig. 12) where a simple model of partial sedimentation in the basins is used.

Model 6 is the same as Model 1 except that sediment is added at a specified rate from a landward source and is

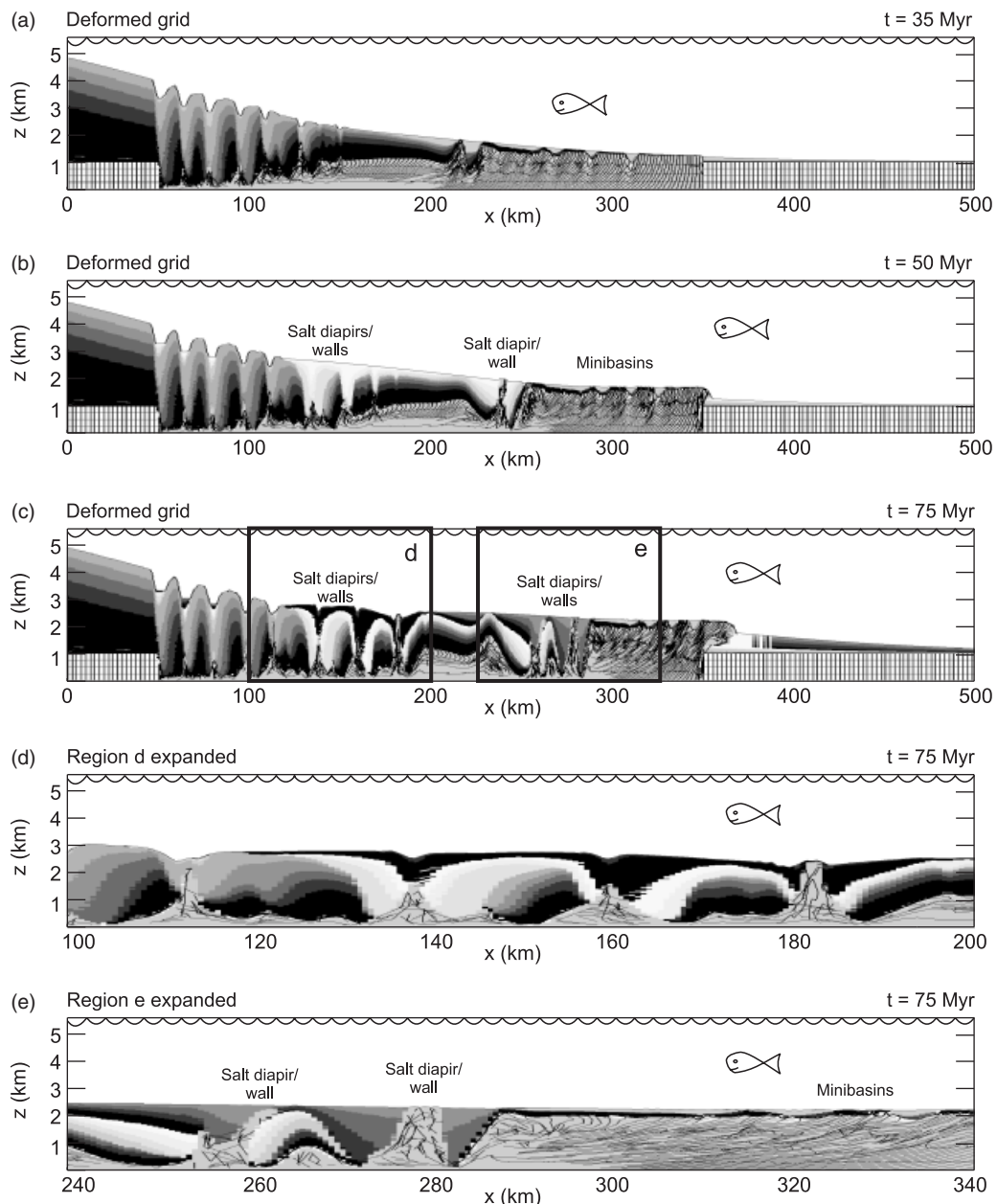


Fig. 12. Model 6. Partial infill of depocentres and reduced sediment input at late stages. Salt is medium grey. Sedimentary overburden is light grey. Deposited sediment is dark to light grey. Each colour corresponds to deposition during 5 Myr. Each cell on the figure corresponds to 4×4 elements in the Lagrangian grid. (a) Model at 35 Myr. (b) Model at 50 Myr. (c) Model at 75 Myr. Vertical exaggeration in (a–c) = 15. (d) Close-up of proximal salt walls and sediment rafts after 75 Myr. (e) Close-up of distal diapirs after 75 Myr. Vertical exaggeration in (d) and (e) = 3 (for link to colour animation, see end of paper).

distributed such that shelf and slope basins are sequentially filled to a level that is 500 m below their spill level, the barrier height on the seaward side of the local basin. Only basins that have a spill level higher than 2500 m are filled in this manner. Sediment deposited in the basins is subtracted from the budget and any residual sediment is deposited as a prograding wedge seaward of the last partially filled basin. This wedge has a profile that follows the same half-Gaussian function as the previous models (Eqn. (33)). h_1 is the height of the last basin barrier and x_1 is chosen so that the total sediment budget is constant at $12.5 \text{ m}^2 \text{ yr}^{-1}$ per unit strike length of the model. At 30 Myr this sediment budget is reduced to $2.5 \text{ m}^2 \text{ yr}^{-1}$ to simulate a period of low sediment flux.

At 35 Myr (Fig. 12a) the landward extensional depocentres start to develop seaward bathymetric barriers and small, underfilled troughs develop where the surface is subsiding. The sediment budget model causes faster progradation during early model stages and a steeper overburden transition zone than for the previous models, which suppresses the development of minibasins. In this model, the landward salt diapirism arising from the local differential pressures also becomes increasingly pronounced in the seaward direction where the salt layer remains sufficiently thick to feed the diapirs (Fig. 12b; $x = 100\text{--}150$ km). Continued extension complemented by growth of the diapirs (75 Myr; Fig. 12c, d) leads to partially filled basins overlying salt diapirs. Diapir growth is limited by the supply of salt to the diapirs and the differential pressures which both decrease with time and lead to reduced velocities. The main difference between this model and the model with sediment aggradation (Model 5) is that the partially filled landward basins maintain local differential pressures, thereby causing continued diapirism instead of falling of the diapirs at late model stages.

In the seaward region, the low progradation profile (smaller h_1 compared with Model 1, for example) results in an aggradational sedimentation pattern, which allows salt diapirs to grow with the aggrading sediment in between the already existing minibasins (Fig. 12b, $x = 240$ km). The rising salt acts as a weak zone along which listric growth faults form (Fig. 12e, $x = 280$ km). Distal sedimentation prevents the development of a large salt nappe and, instead, causes the evacuated salt to move subvertically at its seaward depositional limit in the same way as Model 5.

DISCUSSION

Effects of water loading and pore fluid pressures in nature, and in numerical and analogue models

Analytical and numerical models are useful in the investigation of processes that determine the evolution of passive continental margin sedimentary basins that contain salt. Differential sediment loading pumps the salt seaward, and under some circumstances the sedimentary overburden fails by landward extension and seaward contraction.

The failure analysis emphasises the need to take into account the effects of water loading and pore-fluid pressures when quantifying the failure limit and the post-failure velocities of these systems. The water column increases the solid and fluid pressures in the sediments and reduces the differential pressure in the salt caused by prograding sediments. In addition, the water applies a horizontal force that buttresses and helps stabilise the sloping overburden.

Most published numerical models of salt tectonics (e.g. Gemmer *et al.*, 2004) approximate the effects of pore fluid pressure by using an effective angle of friction of the sedimentary overburden that is lower than the internal angle of friction for dry sediment material. Considering the uncertainties in nature in regard to sediment properties, initial geometry of the system, and the effects of sedimentation and permeability and associated seepage flow on pore-fluid pressures, this approach may be a useful first approximation to investigate the sensitivity of the system to fluid pressures. In addition, as shown in Figs 4 and 5, the failure limit and velocities of continental margin salt tectonic systems investigated in this paper depend significantly on whether the basin is subaerial or submarine. In particular, the marine buttress force acting on the water-sediment interface acts on the overburden transition zone, stabilises the system, and reduces the post-failure velocities. The seaward flow of overburden and salt may be overestimated by about a factor of three in models that do not consider the effects of the water column (Fig. 5; cf. Case 1, no water load, $\phi_{\text{eff}} = 16.42^\circ$ with Case 2).

Similar problems exist with analogue models. Although pore fluid pressure effects have been included in some experiments (Cobbold *et al.*, 2001a; Vendeville & Gaullier, 2003), most analogue models of salt tectonics use materials like dry sand to approximate Coulomb-type overburden and do not include water loading. A comparison of Model 1 (submarine) and Model 2 (subaerial) shows that the higher velocities of the subaerial model lead to overburden extension even for small overburden thicknesses and suppress the formation of minibasins. Thus, although the overall pattern of landward extension and seaward salt evacuation characterises both systems, the dry system fails to develop some of the local salt tectonic structures, such as minibasins in the seaward region.

Insight gained from the numerical models

Model 1 shows that a simple 2D model of smoothly prograding sediments above a rectangular 2D cross section salt layer produces many basic features observed in natural salt tectonic systems. Models with more complex geometries can easily be designed but the intention here has been to focus on some of the basic physical processes and to ask which of these result in significant salt structures without appealing to complex initial geometries. For example, in Model 1 smooth sediment progradation above a uniform thickness viscous salt layer first results in minibasin formation. No appeal to irregularities in sedimentation pattern or salt geometry is required. Continued sediment

progradation leads to extensional failure of the landward section and the minibasins formed during the early stages become part of the rafts located in between the extensional depocentres. The development of minibasins depends, among other things, on the initial thickness of the sedimentary overburden, the sediment progradation rate and the component of sediment aggradation. In a previous study Gemmer *et al.* (2004) used a relatively thick (500 m) initial sedimentary overburden and a more aggressive sediment progradation model (faster progradation rate and a narrower overburden transition zone). These models produced seaward contractional salt-cored folds, not minibasins, indicating that the formation of minibasins is favoured when the initial sediment thickness and the sediment progradation rates are small.

Strain-dependent sediment weakening localises the landward deformation along asymmetric listric normal faults, increases the post-failure velocities and leads to faster development salt tectonic structures. The seaward region is less significantly modified by strain softening during the earlier phases of model evolution because the strain, and hence the effect of strain-dependent weakening is smaller here. The strain-softening model presented in this paper is only one example of strain-dependent sediment weakening. The absolute amount of weakening and the strain interval over which weakening occurs in sedimentary basins may vary. We tested the sensitivity of the system to the amount of strain dependent weakening as well as to the strain interval over which strain softening occurs. In general, a smaller amount of strain weakening leads to less localisation. However, the system is less sensitive to, e.g. a doubling of the strain interval over which weakening occurs; once localisation is initiated along a shear zone, the strain increases rapidly and full sediment weakening is obtained over a short time interval as a consequence of the strong positive feedback between localisation and softening. Although variations occur, the asymmetric landward extensional basins and enhanced velocities are general characteristics of systems with strain softening of the sediments. The number of listric faults developed in the numerical model is smaller than is observed in typical continental margin basins (e.g. Fig. 1). This difference is due, among other things, to the simple sedimentation model, which only includes one progradation phase and a smooth progradation profile.

The simple smooth sediment progradation used in Models 1–3 lacks the natural complexity associated with clastic sedimentation on typical rifted continental margins over intervals of more than 100 Myr (e.g. Fig. 1). Models 4–6 show how salt tectonics may be modified by simple time-space variations in sedimentation. Regional differential pressures caused by the overburden are the primary cause of lateral long-range salt flow leading to evacuation of the landward region and accumulation and thickening of the salt in the seaward region. Situations where sediment progradation only creates a long-range pressure gradient (e.g. Model 1) lead to some salt diapirism but, as

demonstrated in Models 4–6, the diapirism is significantly enhanced when local pressure gradients occur.

Although our current 2D models cannot reproduce the complexity of planform sediment routing and dispersal, we can infer that diapirism is likely enhanced during periods of low sediment influx and when the overburden remains unstable, if these factors combine to give bathymetric variability that creates local pressure gradients that act on the salt. Total sediment starvation also limits the growth potential of the diapirs but slow sedimentation rates comparable to rates of vertical salt movement can maximise passive salt diapirism. The timing of intervals of slow sedimentation in relation to salt evacuation is crucial. If the salt has already been evacuated by the regional pressure gradient during earlier phases of large-scale sediment progradation only salt pillows may remain and significant new diapirism is precluded.

The sediment bypass model presented in this paper prescribes the filling of the proximal depocentres up to 500 m below the barrier height, which results in relatively limited sedimentation in the depocentres. A 500-m deep depocentre may be reasonable if bypass is attributed to efficient transport through incised canyons and levee complexes. However, if sediment bypass is associated with fill-and-spill systems (e.g. Sinclair & Tomasso, 2002) filling to within 100 m of the barrier height may be more realistic. This more complete filling would reduce the local differential pressures and thereby reduce the rate of diapir growth, but may lead to significant passive growth if the sedimentation rates are less than the diapir growth rates. It may only be necessary for there to be a relatively short interval of significant underfilling of an extensional basin to initiate diapirism (*cf.* Model 4; Fig. 10b). Once initiated by local pressure gradients the effect of buoyancy becomes more significant as the height of the diapir increases. Later diapiric growth may be entirely driven by buoyancy, in which no local variations in sedimentation are required for diapirism to continue.

The models presented in this paper show how the evolution of passive margin salt tectonic systems depends on sediment properties and sedimentation patterns. The parameters investigated here represent only a small fraction of the range of salt tectonic systems that may be observed in nature. In previous studies (Gemmer *et al.*, 2004; Ings *et al.*, 2004) we showed how other parameters, e.g. sediment progradation rate, width and thickness of the salt layer, density distribution as well as regional tectonic processes such as thermal subsidence following rifting and isostatic compensation of the sediment column may have a significant impact on the evolution of the system. Other factors that may affect the systems are a superimposed regional stress field, variations in basement and salt geometry, sediment compaction, and the rheology of the salt. We aim to assess effects of some of these parameters in later studies.

CONCLUSIONS

The structural evolution of passive continental margin sedimentary basins that contain salt has been investigated

using analytical and numerical models of a viscous salt layer overlain by a frictional–plastic sedimentary overburden of laterally varying thickness. Differential sediment load on the viscous salt layer leads to a pressure-driven Poiseuille flow, and under some circumstances results in failure of the sedimentary overburden by landward extension accommodated by seaward contraction. We have estimated the failure limit and post-failure velocities of the system from analytical thin sheet calculations that take into account the effects of water loading and pore fluid pressures in the sediments. The overburden velocities depend on the overburden strength, the thicknesses of the overburden and the viscous layer and on the width of the transition zone over which the overburden thickness varies. Water loading increases the solid and fluid pressures of the sedimentary overburden and reduces the differential pressure in the salt. In addition, the water exerts a pressure that is normal to the sediment surface. This leads to velocities of the submarine systems that are about a factor 2 smaller than for the equivalent subaerial system.

The finite-element model reproduces the pattern of landward extension accommodated by seaward contraction observed in numerous sedimentary basins on continental margins. When the sedimentary overburden is thin, sediment progradation above a viscous salt layer initially leads to minibasin formation. Continued sediment progradation results in the formation of landward extensional basins and seaward contraction, and the development of salt diapirs with intervening minibasins. The tectonic structures depend on the sediment properties and the sedimentation patterns. Strain-dependent weakening of the frictional sedimentary overburden leads to localisation of deformation along shear zones and causes landward asymmetric extensional depocentres bounded by listric growth shears. Periods of sediment starvation and sediment bypass result in local differential pressures that force salt diapirism in the shelf region. Sediment aggradation allows for salt diapirs to grow passively with the aggrading sediment. Such investigations of the dynamics of salt tectonics at passive continental margins may improve data interpretations and basin analysis, and hence advance our quantitative understanding of these systems.

ACKNOWLEDGEMENTS

We wish to thank R. Fletcher, B. Vendeville, R. Mourgues and D. Waltham for constructive reviews and John Shimeld for fruitful discussions on observed salt structures. This research is funded by an ACOA – Atlantic Innovation Fund contract, and an IBM–Shared University Research Grant. L. Gemmer was supported by the Danish Natural Science Research Council and the Carlsberg Foundation. Chris Beaumont was supported by the Canada Research Chair in Geodynamics. S. Ings was supported by NSERC and NRCan Scholarships.

REFERENCES

- COBBOLD, P.R., DURAND, S. & MOURGUES, R. (2001a) Sandbox modelling of thrust wedges with fluid-assisted detachments. *Tectonophysics*, **334**, 245–258.
- COBBOLD, P.R., MEISLING, K.E. & MOUNT, V.S. (2001b) Reactivation of an obliquely rifted margin, Campos and Santos basins, southeastern Brazil. *AAPG Bull.*, **85**, 1925–1944.
- COHEN, H.A. & HARDY, S. (1996) Numerical modelling of stratal architectures resulting from differential loading of a mobile substrate. In: *Salt tectonics* (Ed. by G.I. Alsop, D.J. Blundell & I. Davison), *Geol. Soc. London. Spec. Publ.*, **100**, 265–273.
- COTTON, J.T. & KOYI, H.A. (2000) Modeling of thrust fronts above ductile and frictional detachments: application to structures in the Salt Range and Potwar Plateau, Pakistan. *GS&A Bull.*, **112**, 351–363.
- DAHLEN, F.A. (1990) Critical taper model of fold-and-thrust belts and accretionary wedges. *Ann. Rev. Earth Planet. Sci.*, **18**, 55–99.
- DEMERICIAN, S., SZATMARI, P. & COBBOLD, P.R. (1993) Style and pattern of salt diapirs due to thin-skinned gravitational gliding, Campos and Santos basins, offshore Brazil. *Tectonophysics*, **228**, 393–433.
- DIEGEL, F.A., KARLO, J.F., SCHUSTER, D.C., SHOUP, R.C. & TAUVERS, P.R. (1995) Cenozoic structural evolution and tectono-stratigraphic framework of the northern Gulf Coast continental margin. In: *Salt tectonics: a global perspective* (Ed. by M.P.A. Jackson, D.G. Roberts & S. Snelson), *AAPG Mem.*, **65**, 109–151.
- DUGAN, B. & FLEMINGS, P.B. (2000) Overpressure and fluid flow in the New Jersey Continental Slope: implications for Slope Failure and Cold Seeps. *Science*, **289**, 288–291.
- DUVAL, B., CRAMEZ, C. & JACKSON, M.P.A. (1992) Raft tectonics in the Kwanza Basin, Angola. *Mar. Petrol. Geol.*, **9**, 389–404.
- FLEMINGS, P.B., STUMP, B.B., FINKBEINER, T. & ZOBACK, M. (2002) Flow focusing in overpressured sandstones: theory, observations, and applications. *Am. J. Sci.*, **302**, 827–855.
- FLETCHER, R.C., HUDEC, M.R. & WATSON, I.A. (1995) Salt glacier and composite sediment-salt glacier models for the emplacement and early burial of allochthonous salt sheets. In: *Salt tectonics: a global perspective* (Ed. by M.P.A. Jackson, D.G. Roberts & S. Snelson), *AAPG Mem.*, **65**, 77–108.
- FULLSACK, P. (1995) An arbitrary Lagrangian–Eulerian formulation for creeping flows and its applications in tectonic models. *Geophys. J. Int.*, **120**, 1–23.
- GE, H., JACKSON, M.P.A., VENDEVILLE, B.C., MALER, M.O. & HANDSCHY, W. (1997) Deformation of prograding wedges over a ductile layer – application of physical models to geologic examples. *Gulf Coast Assoc. Geol. Soc. Trans.*, **XLVII**, 177–184.
- GEMMER, L., SINGS, S.J., MEDVEDEV, S. & BEAUMONT, C. (2004) Salt tectonics driven by differential sediment loading: stability analysis and finite element experiments. *Basin Res.*, **16**, 199–218.
- HART, B.S., FLEMINGS, P.B. & DESHPANDE, A. (1995) Porosity and pressure: role of compaction disequilibrium in the development of geopressures in a Gulf Coast Pleistocene basin. *Geology*, **23**, 45–48.
- HUBBERT, M.K. & RUBEY, W.W. (1959) Role of fluid pressure in mechanics of overthrust faulting. 1. Mechanics of fluid-filled porous solids and its application to overthrust faulting. *Geol. Soc. Am. Bull.*, **70**, 115–166.
- INGS, S.J., BEAUMONT, C. & GEMMER, L. (2004) Numerical modeling of salt tectonics on passive continental margins: pre-

- liminary assessment of the effects of sediment loading, buoyancy, margin tilt, and isostasy. *2004 GCSSEPM Foundation Bob F. Perkins Research Conference papers* (on CD).
- KIDSTON, A.G., BROWN, D.E., ALTHEIM, B. & SMITH, B.M. (2002) *Hydrocarbon Potential of the Deep-Water Scotian Slope*. Canada-Nova Scotia Offshore Petroleum Board, Halifax, Canada.
- KIRBY, S.H. (1985) Rock mechanics observations pertinent to the rheology of the continental lithosphere and the localization of strain along shear zones. *Tectonophysics*, **119**, 1–27.
- KOYI, H. (1996) Salt flow by aggrading and prograding overburdens. In: *Salt Tectonics* (Ed. by G.I. Alsop, D.J. Blundell & I. Davison), *Geol. Soc. Spec. Publ.*, **100**, 243–258.
- LAST, N.C. (1988) Deformation of a sedimentary overburden on a slowly creeping substratum (Innsbruck 1988). In: *Numerical Methods in Geomechanics* (Ed. by G. S. Swoboda), pp. 577–585. Balkema, Rotterdam.
- LEHNER, F.K. (1977) A theory of subratral creep under varying overburden with applications to tectonics. AGU Spring Meeting, Washington D.C.. *EOS Abstr.*, **58**, 508.
- LEHNER, F.K. (2000) Approximate theory of substratum creep and associated overburden deformation in salt basins and deltas. In: *Aspects of Tectonic Faulting* (Ed. by F.K. Lehner & J.L. Urai), pp. 21–47. Springer-Verlag, Berlin.
- LOBKOVSKY, L.I. & KERCHMAN, V.I. (1991) A two-level concept of plate tectonics: application to geodynamics. *Tectonophysics*, **199**, 343–374.
- LUPA, J., FLEMINGS, P. & TENNANT, S. (2002) Pressure and trap integrity in the deepwater Gulf of Mexico. *The Leading Edge*, **21**, 184–187.
- MARTON, L.G., TARI, G.C. & LEHMANN, C.T. (2000) Evolution of the Angolan passive margin, West Africa, with emphasis on post-salt structural styles. In: *Atlantic rifts and continental margins* (Ed. by W. Mohriak & M. Talwani), *Am. Geophys. Union Geophys. Monogr.*, **115**, 129–149.
- MODICA, C.J. & BRUSH, E.R. (2004) Postrift sequence stratigraphy, paleogeography, and fill history of the deep-water Santos Basin, offshore southeast Brazil. *AAPG Bull.*, **88**, 923–945.
- MOURGUES, R. & COBBOLD, P.R. (2003) Some tectonic consequences of fluid overpressures and seepage forces as demonstrated by sandbox modelling. *Tectonophysics*, **376**, 75–97.
- PEEL, F.J., TRAVIS, C.J. & HOSSACK, J.R. (1995) Genetic structural provinces and salt tectonics of the Cenozoic Offshore U.S. Gulf of Mexico: a preliminary analysis. In: *Salt tectonics: a global perspective* (Ed. by M.P.A. Jackson, D.G. Roberts & S. Snelson), *AAPG Mem.*, **65**, 153–175.
- ROWAN, M.G., TRUDGILL, B.D. & FIDUK, J.C. (2000) Deep-water, salt-cored foldbelts: lessons from the Mississippi Fan and Perdido foldbelts, northern Gulf of Mexico. In: *Atlantic rifts and continental margins* (Ed. by W. Mohriak & M. Talwani), *Am. Geophys. Union Geophys. Monogr.*, **115**, 173–191.
- SHIMELD, J. (2004) A comparison of salt tectonic sub-provinces beneath the Scotian Slope and Laurentian Fan: *GCSSEPM 24th Bob F. Perkins Research Conference Proceedings* (on CD).
- SINCLAIR, H.D. & TOMASSO, M. (2002) Depositional evolution of confined turbidite basins. *J. Sediment. Res.*, **72**, 451–456.
- TARI, G.C., ASHTON, P.R., COTERILL, K.L., MOLNAR, J.S., SORGENFRIE, M.C., THOMPSON, P.W.A., VALASEK, D.W. & FOX, J.F. (2002) Are West Africa deepwater salt tectonics analogues to the Gulf of Mexico? *Oil Gas J.*, **4**, 73–81.
- VON TERZAGHI, K. (1923) Die Berechnung der Durchlässigkeitsziffer des Tonen aus dem Verlauf der hydrodynamischen Spannungsscheinungen. *Szgeber. Akad. Wiss. Wien Math-Naturwiss. Klasse IIa*, **132**, 125–138.
- TRUDGILL, B.D., ROWAN, M.G., FIDUK, J.C., WEIMER, P., GALE, P.E., KORN, B.E., PHAIR, R.L., GAFFORD, W.T., ROBERTS, G.R. & DOBBS, S.W. (1999) The Perdido fold belt, northwestern deep Gulf of Mexico, part 1: structural geometry, evolution and regional implications. *AAPG Bull.*, **83**, 88–113.
- VENDEVILLE, B.C. & GAULLIER, V. (2003) Role of pore-fluid pressure and slope angle in triggering submarine mass movements: natural examples and pilot experimental models. In: *Submarine mass movements and their consequences* (Ed. by J. Locat & J. Mienert), pp. 137–144. First International Symposium. Kluwer Academic Publishers, Dordrecht, Netherlands.
- VENDEVILLE, B.C. & JACKSON, M.P.A. (1992) The rise of diapirs during thin-skinned extension. *Mar. Petrol. Geol.*, **9**, 331–353.
- WADE, J.A. & MACLEAN, B.C. (1990) The geology of the southeastern margin of Canada, Chapter 5. In: *Geology of the Continental Margin of Eastern Canada* (Ed. by M.J. Keen & G.L. Williams), *Geol. Survey Canada Geol. Canada*, **2**, 167–238 (also Geological Society of America, the Geology of North America, Vol. I-1).
- WILLETT, S.D. (1999) Rheological dependence of extension in wedge models of convergent orogens. *Tectonophysics*, **305**, 419–435.
- WORRALL, D.M. & SNELSON, S. (1989) Evolution of the northern Gulf of Mexico, with emphasis on Cenozoic growth faulting and the role of salt. In: *The Geology of North America: an overview*, vol. A (Ed. by A.W. Bally & A.R. Palmer), pp. 97–138. Geological Society of America, The Geology of North America, Boulder, CO.
- WU, S., BALLY, A. & CRAMEZ, C. (1990) Allochthonous salt, structure and stratigraphy of the north-eastern Gulf of Mexico. Part II: structure. *Mar. Petrol. Geol.*, **7**, 334–370.
- YASSIR, N.A. & BELL, J.S. (1994) Relationships between pore pressure, stresses and present-day geodynamics in the Scotian Shelf, Offshore Eastern Canada. *AAPG Bull.*, **78**, 1863–1880.

Manuscript received 6 January 2005; Manuscript accepted 29 July 2005

SUPPLEMENTARY INFORMATION

Supplementary information accompanies the paper on the Dalhousie Geodynamics Group salt web site (<http://geodynam.ocean.dal.ca/salt/basinrespaper2.html>).